

Banner appropriate to article type will appear here in typeset article

# Turbulent disruption of density staircases in stratified shear flows

Nicolaos Petropoulos<sup>1†</sup>, Ali Mashayek<sup>2</sup> and Colm-cille P. Caulfield<sup>3,1</sup>

<sup>1</sup>Department of Applied Mathematics and Theoretical Physics, University of Cambridge, Cambridge CB3 0WA, UK

<sup>2</sup>Department of Civil and Environmental Engineering, Imperial College London, London SW7 2BX, UK

<sup>3</sup>BP Institute, University of Cambridge, Cambridge CB3 0EZ, UK

(Received xx; revised xx; accepted xx)

Formation of step-like ‘density staircase’ distributions induced by stratification and turbulence has been widely studied and can be explained by the ‘instability’ of a sufficiently strongly stably stratified turbulent flow due to the decrease of the turbulent density flux with increasing stratification via the ‘Phillips mechanism’ (Phillips 1972). However, such density staircases are not often observed in ocean interiors, except in regions where double diffusion processes are important, leading to thermohaline staircases. Using reduced order models for the evolution of velocity and density gradients, we analyse staircase formation in stratified and sheared turbulent flows. Under the assumption of inertial scaling  $\epsilon \sim U^3/L$  for the kinetic energy dissipation rate  $\epsilon$ , where  $U$  and  $L$  are characteristic velocity and length scales, we determine ranges of bulk Richardson numbers  $Ri_b$  and turbulent Prandtl numbers  $Pr_T$  for which staircases can potentially form and show that the Phillips mechanism only survives in the limit of sufficiently small turbulent Prandtl numbers. For relevant oceanic parameters, a limit turbulent Prandtl number above which the system is not prone to staircases is found to be  $Pr_T \approx 0.5 - 0.7$ . Since several studies indicate that the turbulent Prandtl number in stably stratified turbulence and in ocean interiors is usually above this threshold, this result supports the empirical observation that staircases are not favoured in ocean interiors in the presence of ambient turbulence. We also show that our analysis is robust to other scalings for  $\epsilon$  (such as the more strongly stratified scaling  $\epsilon \sim U^2 \bar{N}$ , where  $\bar{N}$  is a characteristic value of the buoyancy frequency), supporting our results in both shear-dominated and buoyancy-dominated turbulent regimes as well as in weakly and strongly stratified regimes.

## 1. Introduction

Spontaneous formation of step-like ‘density staircases’ distributions – made up of a series of relatively deep and well-mixed ‘layers’ separated by relatively thin ‘interfaces’ of enhanced density gradient – induced by stratification and turbulence has been postulated and studied by many authors (Phillips 1972; Posmentier 1977) and has been observed in a number of contexts. Experimentally, density staircases form when dragging a rod or a grid through a stable salt gradient (Linden 1980; Thorpe 1982; Ruddick *et al.* 1989) or in stratified turbulent Taylor-Couette flows (Ogletorpe *et al.* 2013). In the oceans, they

† Email address for correspondence: np546@cam.ac.uk

have been detected in regions where double-diffusion is important (in polar regions for example) and leads to the development of thermohaline staircases (Timmermans *et al.* 2008; Radko 2016). In the Arctic, their presence is crucial, not least because they act as a barrier to mixing, protecting the Arctic ice from the heat input inflowing from the Atlantic ocean (Rippeth & Fine 2022). In astrophysical stratified flows, density staircases could potentially form in regions with sufficiently large molecular Prandtl number ( $O(10^{-3})$  or larger; in white dwarf interiors for example) thanks to fingering convection (Garaud *et al.* 2015). The formation of such structures is due to the interaction between small scale turbulence and larger scale stratification. Such turbulence is inherently anisotropic as stratification tends to inhibit vertical motions, and inhomogeneous due to the inevitable presence of sharp density interfaces.

Although stratified turbulence is thus inevitably difficult to analyse, insight has been gained using flux-gradient parameterisations. Using such models, Phillips (1972) and Posmentier (1977) reduced the dynamics of the staircase formation problem (with a single stratification agent) to the following nonlinear diffusion equation for the horizontally averaged buoyancy  $\bar{b}$ :

$$\partial_t \bar{b} = \partial_z [F(\partial_z \bar{b})], \quad (1.1)$$

where, importantly, the turbulent buoyancy flux  $F$  is a non-monotonic function of the buoyancy gradient (Linden 1979). Using this formulation, layering can be explained by an ‘instability’ of a sufficiently strongly stably stratified turbulent flow due to the decrease of the turbulent buoyancy flux with increasing stratification, through what is now commonly referred to as the ‘Phillips mechanism’. Flux-gradient parameterisations have, however, some drawbacks. Firstly, they are antidiffusive when the flux is a decreasing function of the gradient, leading to mathematically ill-posed problems, and it is this ill-posedness which manifests itself as the ‘instability’ of the Phillips mechanism. Secondly, they are not valid at all scales and tend to break down when the size of the phenomenon of interest (the layers in our case) is of the order of magnitude or smaller of the turbulent microstructures that such models try to parameterise (Radko 2014). These issues can both be resolved using the recently developed multi-scale analysis introduced by Radko (2019) in the context of thermohaline layering. Carefully introducing the interplay between different scales into the flux-gradient parameterisations, this method corrects the models at small scales and generates mathematically well-posed systems. Other regularisation techniques have also been proposed. Barenblatt *et al.* (1993) used a time-delayed flux-gradient model to construct a mathematically well-posed model of mixing in stratified turbulent flows whereas Balmforth *et al.* (1998) considered the evolution of both buoyancy gradients and turbulent kinetic energy to analyse staircase dynamics in stratified turbulent flows.

The above reduced order model predicts layer formation for sufficiently strongly stratified flows. Furthermore, Billant & Chomaz (2001) identified a strongly stratified regime (in the sense that the horizontal Froude  $Fr_h = U/L_h \bar{N}$  number is small, where  $U$  is a characteristic horizontal velocity scale,  $L_h$  is a typical horizontal length scale, and  $\bar{N}$  is a characteristic value of the buoyancy frequency) for which the (full) equations of motion are self-similar with respect to  $z\bar{N}/U$ , suggesting a layered structure with characteristic vertical length scale  $U/\bar{N}$ . This vertical layering offers a route for turbulence to grow and be sustained in strongly stratified flows and hence mix strong density gradients. Indeed, whereas sufficiently weakly stratified flows are prone to shear instabilities that can overturn density gradient, strongly stratified flows prevent such instabilities from growing. However, they are prone to layering that reduces (locally) the stratification inside the layers, creating a favourable environment for shear instabilities to develop (Cope *et al.* 2020). The subsequent turbulence is inevitably spatially and temporally intermittent and is characterised by scouring dynamics

near the relatively sharp density interfaces rather than overturns, emphasizing the qualitatively different mixing expected in relatively weakly or strongly stratified flows (Woods *et al.* 2010; Caulfield 2021).

Oceanic flows are indeed often exceptionally strongly stratified (Riley & Lelong 2000; Thorpe 2005) and layering should on the face of it therefore play an important role to mix density gradients. However, perhaps surprisingly, density staircases are not often observed in oceans interiors except when thermohaline diffusion is playing a prominent role. Motivated by this somewhat curious observation, we analyse staircase formation in both density stratified and sheared turbulent flows and assess in which regime(s) it is possible for the Phillips mechanism to survive. Using reduced order models for the evolution of velocity and density gradients based on flux-gradient parameterisations of the turbulent fluxes (corrected using a simpler version of Radko (2019) multi-scale analysis) and under various scalings for the rate of dissipation of the kinetic energy  $\epsilon$  (specifically  $\epsilon \sim U^3/L$  and  $\epsilon \sim U^2\bar{N}$  where  $L$  is a characteristic length-scale of our problem), we determine ranges of bulk Richardson numbers  $Ri_b$  and turbulent Prandtl numbers  $Pr_T$  (defined more precisely below, effectively quantifying the relative strength of velocity shear to the buoyancy frequency and the ratio of turbulent diffusivity of momentum to turbulent diffusivity of buoyancy respectively) for which staircases can potentially form.

We demonstrate conclusively that the Phillips mechanism for layer formation in strongly stratified flows remains viable in the presence of shear only in the limit  $Pr_T \ll 1$  but breaks down otherwise. Specifically, for sufficiently large  $Ri_b \gtrsim 1$  there exists a limiting value of the turbulent Prandtl number  $Pr_T$  above which layering via this mechanism ceases to be possible. For relevant oceanic parameters, this value is found around 0.5 – 0.7. Even though it is still challenging to measure the turbulent Prandtl number in the oceans, several studies of direct numerical simulation of stably stratified turbulence indicate that  $Pr_T$  is typically non-trivially above this threshold (Shih *et al.* 2005; Venayagamoorthy & Stretch 2010) and therefore our result supports and explains the empirical observation that staircases are not favoured in ocean interiors in the presence of ambient turbulence driven by velocity shears.

To demonstrate this key result, the rest of the paper is organised as follows. In section 2 we introduce the theoretical model used throughout the paper to analyse staircase formation in both density (stably) stratified and sheared turbulent flows, through extending the work of Phillips (1972) and Posmentier (1977) to take into account the evolution of shear, and define relevant dimensionless parameters. In section 3 we describe the regions in parameter space that are prone to staircase instabilities through a linear stability analysis of the governing equations. In section 4 we present some properties of the various instabilities, while in section 5 we compare the nonlinear dynamics leading to layer formation and the stability analyses. Finally, we draw brief conclusions in section 6.

## 2. Formulation

### 2.1. Dimensional form

The Navier-Stokes equations in the Boussinesq approximation (with a background density  $\rho_0$ ) and hydrostatic balance are:

$$\begin{cases} \partial_t u + \mathbf{u} \cdot \nabla u = \nu_m \nabla^2 u - \frac{1}{\rho_0} \partial_x p, & \partial_t v + \mathbf{u} \cdot \nabla v = \nu_m \nabla^2 v - \frac{1}{\rho_0} \partial_y p, \\ \frac{1}{\rho_0} \partial_z p = b, & \partial_t b + \mathbf{u} \cdot \nabla b = \kappa_m \nabla^2 b, & \nabla \cdot \mathbf{u} = 0, \end{cases} \quad (2.1)$$

where  $\mathbf{u} = (u, v, w)$  is the velocity field,  $b$  is buoyancy,  $p$  is pressure and  $\kappa_m$  and  $\nu_m$  are the (molecular) diffusivity and viscosity of the fluid. Averaging in the horizontal and assuming that  $\mathbf{u} = (\bar{u}(z, t), 0, 0) + \mathbf{u}'$  and  $b = \bar{b}(z, t) + b'$  where  $\bar{u}$  and  $\bar{b}$  are the horizontally averaged

velocity and buoyancy respectively, we obtain:

$$\begin{cases} \partial_t \bar{b} = \kappa_m \partial_{zz} \bar{b} - \partial_z F_b, & F_b = \overline{b'w'}, \\ \partial_t \bar{u} = \nu_m \partial_{zz} \bar{u} - \partial_z F_u, & F_u = \overline{u'w'}, \end{cases} \quad (2.2)$$

where  $F_b$  and  $F_u$  are respectively the vertical buoyancy and momentum turbulent fluxes. Using gradient-flux models to parameterise these fluxes in terms of the mean buoyancy and velocity gradients we obtain implicit definitions for the turbulent diffusivities of buoyancy  $\kappa_T$  and momentum  $\nu_T$ :

$$F_b = -\kappa_T \partial_z \bar{b}, \quad F_u = -\nu_T \partial_z \bar{u}. \quad (2.3)$$

Our goal is to understand how an ambient shear influences the formation of density (or equivalently buoyancy) staircases. Therefore, we choose to model these fluxes only in terms of the gradient Richardson number  $Ri$ , defined in terms of the background shear  $S$  and buoyancy frequency  $N$ :

$$Ri := \frac{N^2}{S^2}; \quad S := \partial_z \bar{u}, \quad N^2 := \partial_z \bar{b}. \quad (2.4)$$

It is important to remember that common parameterisations of the turbulent diffusivities rely also on the buoyancy Reynolds number  $Re_b = \epsilon/\nu_m N^2$  where  $\epsilon$  is the dissipation rate of turbulent kinetic energy (Shih *et al.* 2005; Bouffard & Boegman 2013; Mashayek *et al.* 2017). We can however express the buoyancy flux as:

$$F_b = -\Gamma \epsilon, \quad (2.5)$$

where  $\Gamma$  is the turbulent flux coefficient (Osborn 1980) and reduce the modeling of the turbulent diffusivities  $\kappa_T$  and  $\nu_T$  to the modeling of this coefficient. Parameterisations of  $\Gamma$  in terms of  $Ri$  have been presented (Wells *et al.* 2010). At  $Ri = 0$ , there is no buoyancy to mix and therefore it seems reasonable to assume  $\Gamma(Ri = 0) = 0$ . As  $Ri$  increases, there is more and more scalar to mix and  $\Gamma$  should therefore increase. However, as stratification becomes more significant, it is reasonable to suppose that it will suppress vertical motion, possibly leading to less efficient mixing. Whether  $\Gamma$  decreases or saturates for  $Ri$  large enough is still an open question (Caulfield 2021). However, the analysis presented in the following sections depends most strongly on the monotonicity of the flux coefficient in terms of the Richardson number, and not the specific functional form of  $\Gamma(Ri)$  and hence the two cases can be studied, as we will see later.

Written in terms of the flux coefficient  $\Gamma$ , the mean buoyancy and velocity equations (2.2) are:

$$\begin{cases} \partial_t N^2 = \kappa_m \partial_{zz} N^2 + \partial_{zz} [\Gamma \epsilon], \\ \partial_t S = \nu_m \partial_{zz} S + Pr_T \partial_{zz} \left[ \frac{\Gamma \epsilon}{SRi} \right], & Pr_T := \frac{\nu_T}{\kappa_T}, \end{cases} \quad (2.6)$$

where for the sake of simplicity and because we want to understand how this parameter affects the formation of staircases, we consider a constant turbulent Prandtl number  $Pr_T$ . These equations are coupled through the dependence of the flux coefficient  $\Gamma$  on the Richardson number  $Ri$ . For clarity we henceforth drop the overbars on  $b$  and  $u$ .

## 2.2. Dimensionless system

In order to scale the system (2.6), we need to make some assumptions regarding the relevant time-scale of our problem as well as on the dissipation rate of turbulent kinetic energy  $\epsilon$ . Using data from various sources, Mater & Venayagamoorthy (2014) show that stably stratified shear-flow turbulence could be interpreted in terms of three time-scales: the buoyancy time-scale  $T_b = 1/N$ , the shear time-scale  $T_S = 1/S$  and turbulence time-scale  $T_T = \mathcal{K}/\epsilon$  where  $\mathcal{K}$

is the turbulent kinetic energy density. In the following, we propose three different scalings that depend on the relative size of these time-scales.

### 2.2.1. Inertial scaling

We first propose to scale the system (2.6) under the assumption that the dissipation rate of turbulent kinetic energy  $\epsilon$  scales ‘inertially’ like  $U^3/L$  where  $U$  is a characteristic velocity scale and  $L$  is a characteristic length scale of our problem. This scaling has been justified in many experimental and observational settings (Ivey & Imberger 1991; Ivey *et al.* 1998; Kay & Jay 2003; Shih *et al.* 2005). It is relevant, for instance, in sufficiently weakly stratified or shear-dominated turbulent flows where the turbulent Froude number  $\text{Fr}_T := \epsilon/N\mathcal{K}(=T_b/T_T)$  as well as the Froude number  $\text{Fr} := S/N(=T_b/T_S)$  are sufficiently large (Mater & Venayagamoorthy 2014). Then, the relevant time-scale of dissipation of turbulent kinetic energy is set by the shear and  $\epsilon$  scales inertially.

Therefore, we consider the following scaling, where hatted quantities are dimensionless:

$$u = U\hat{u}, \quad z = L\hat{z}, \quad t = \frac{L}{U}\hat{t}, \quad S = \frac{U}{L}\hat{S}, \quad N^2 = \bar{N}^2\hat{N}^2, \quad \epsilon = \frac{U^3}{L}\hat{\epsilon}, \quad (2.7)$$

where the relevant time-scale has been set by the shear,  $\bar{N}^2$  is a typical value of the buoyancy frequency so that  $\hat{N}^2 = \mathcal{O}(1)$  and, since we are assuming that  $\epsilon$  is large enough to sustain an inertial subrange and that the inertial scaling holds,  $\hat{\epsilon} = \mathcal{O}(1)$  (in fact we will assume, when numerically running the model forward in time, that  $\epsilon$  is constant and therefore  $\hat{\epsilon} = 1$  precisely). In practice,  $\bar{N}^2$  and  $U/L$  are the background stratification and shear of the disturbed profiles considered in the linear stability analysis (section 3). System (2.6) then becomes:

$$\begin{cases} \partial_{\hat{t}}\hat{N}^2 = \frac{1}{\text{Pr}_m\text{Re}}\partial_{\hat{z}\hat{z}}\hat{N}^2 + \frac{1}{\text{Ri}_b}\partial_{\hat{z}\hat{z}}[\Gamma(\text{Ri}_b\hat{\text{Ri}})\hat{\epsilon}], \\ \partial_{\hat{t}}\hat{S} = \frac{1}{\text{Re}}\partial_{\hat{z}\hat{z}}\hat{S} + \frac{\text{Pr}_T}{\text{Ri}_b}\partial_{\hat{z}\hat{z}}\left[\frac{\Gamma(\text{Ri}_b\hat{\text{Ri}})\hat{\epsilon}}{\hat{S}\hat{\text{Ri}}}\right], \\ \text{Pr}_m := \frac{\nu_m}{\kappa_m}, \quad \text{Re} := \frac{UL}{\nu_m}, \quad \text{Ri}_b := \frac{\bar{N}^2L^2}{U^2}, \end{cases} \quad (2.8)$$

where the dependence on three dimensionless parameters (the molecular Prandtl number  $\text{Pr}_m$ , the Reynolds number  $\text{Re}$  and the bulk Richardson number  $\text{Ri}_b$ ) is made explicit. These two equations are coupled through  $\hat{\text{Ri}} := \hat{N}^2/\hat{S}^2$ . We expect layering to be favoured at larger  $\text{Pr}_m$  (Taylor & Zhou 2017). For  $\text{Pr}_m = \mathcal{O}(1)$  we can expect layers to be smoothed by diffusion, at least for sufficiently small  $\text{Re}$  (i.e. sufficiently small Péclet number  $\text{Pe} = \text{Pr}_m\text{Re}$ ).

### 2.2.2. Intermediate scaling for moderately stratified flows

Instead of considering the inertial scaling introduced in the previous section, we can alternatively assume that the dissipation rate of turbulent kinetic energy  $\epsilon$  scales as  $U^2\bar{N}$  (with the notation of section 2.2.1). This scaling is relevant, for instance, to moderately or strongly stratified flows in the sense that  $\text{Fr}_T \lesssim 1$  and therefore the turbulent kinetic energy largely dissipates within a buoyancy time scale and hence  $\epsilon \sim U^2\bar{N}$  (Garanaik & Venayagamoorthy 2019). Considering that the flow is moderately stratified in an intermediate flow regime, in the sense that the dominant time scale is still set by the shear (assuming for instance that we are still in a shear-dominated regime and so the shear time scale  $L/U$  is sufficiently small compared to the turbulent time scale  $\mathcal{K}/\epsilon$  and the buoyancy time scale  $1/N$  (Mater & Venayagamoorthy 2014)), the system (2.6) becomes:

$$\begin{cases} \partial_{\hat{t}}\hat{N}^2 = \frac{1}{\text{Pr}_m\text{Re}}\partial_{\hat{z}\hat{z}}\hat{N}^2 + \frac{1}{\sqrt{\text{Ri}_b}}\partial_{\hat{z}\hat{z}}[\Gamma(\text{Ri}_b\hat{\text{Ri}})\hat{\epsilon}], \\ \partial_{\hat{t}}\hat{S} = \frac{1}{\text{Re}}\partial_{\hat{z}\hat{z}}\hat{S} + \frac{\text{Pr}_T}{\sqrt{\text{Ri}_b}}\partial_{\hat{z}\hat{z}}\left[\frac{\Gamma(\text{Ri}_b\hat{\text{Ri}})\hat{\epsilon}}{\hat{S}\hat{\text{Ri}}}\right]. \end{cases} \quad (2.9)$$

This system is equivalent to the one derived using the inertial scaling (system (2.8)) with the mapping  $\sqrt{\text{Ri}_b}\Gamma(\text{Ri}_b\hat{\text{Ri}}) \rightarrow \Gamma(\text{Ri}_b\hat{\text{Ri}})$ . We will discuss the implications of this intermediate scaling below.

### 2.2.3. Strongly stratified scaling

For sufficiently strongly stratified flows, consistently with the strong stratification scaling derived by (Garanaik & Venayagamoorthy 2019) and the buoyancy-dominated regime analysed by (Mater & Venayagamoorthy 2014), we can also assume that the time scale is set by the buoyancy (i.e.  $t = \frac{1}{N}\hat{t}$ ) and obtain:

$$\begin{cases} \sqrt{\text{Ri}_b}\partial_{\hat{t}}\hat{N}^2 = \frac{1}{\text{Pr}_m\text{Re}}\partial_{\hat{z}\hat{z}}\hat{N}^2 + \frac{1}{\sqrt{\text{Ri}_b}}\partial_{\hat{z}\hat{z}}[\Gamma(\text{Ri}_b\hat{\text{Ri}})\hat{\epsilon}], \\ \sqrt{\text{Ri}_b}\partial_{\hat{t}}\hat{S} = \frac{1}{\text{Re}}\partial_{\hat{z}\hat{z}}\hat{S} + \frac{\text{Pr}_T}{\sqrt{\text{Ri}_b}}\partial_{\hat{z}\hat{z}}\left[\frac{\Gamma(\text{Ri}_b\hat{\text{Ri}})\hat{\epsilon}}{\hat{S}\hat{\text{Ri}}}\right]. \end{cases} \quad (2.10)$$

Once again this system is equivalent to system (2.8) with the mappings  $\sqrt{\text{Ri}_b}\Gamma(\text{Ri}_b\hat{\text{Ri}}) \rightarrow \Gamma(\text{Ri}_b\hat{\text{Ri}})$  and  $\sqrt{\text{Ri}_b}\hat{t} \rightarrow \hat{t}$ , and we will also discuss the implications of this strongly stratified scaling below.

### 2.3. Choice of parameterisation for the flux coefficient

In order to solve the system (2.8) numerically, we must choose a specific functional form for the parameterisation of the flux coefficient  $\Gamma$  in terms of the bulk Richardson number  $\text{Ri}_b$ . Experimental and numerical data (Linden 1979; Turner 1968; Wells *et al.* 2010) suggest that  $\Gamma$  is a non-monotonic function of  $\text{Ri}_b$  with  $\Gamma(\text{Ri}_b) \propto \text{Ri}_b$  on the increasing flank of  $\Gamma$  and  $\Gamma(\text{Ri}_b) \propto 1/\text{Ri}_b^p$  (with  $p \geq 0$ ) on the decreasing flank. These scaling regimes may be respected with the functional form:

$$\Gamma(\text{Ri}_b) = A \frac{\text{Ri}_b}{1 + B\text{Ri}_b^{p+1}}, \quad (2.11)$$

where  $A$  and  $B$  are chosen so that the maximum value of  $\Gamma$ , attained when  $\text{Ri}_b = \text{Ri}_b^* \simeq 1$ , is  $\Gamma^* \simeq 0.2 - 0.3$  (Ivey & Imberger 1991). (As we discuss further below, the specific chosen values of  $\Gamma^*$  and  $\text{Ri}_b^*$  do not affect the qualitative results.) Common values for  $p$  are  $p = 1/2$  and  $p = 1$  (Turner 1968; Linden 1980). It should be noted that in what follows we will try to present results that are as general as possible and do not depend strongly on the precise formulation (2.11) of  $\Gamma$  but only on its monotonicity and asymptotic rate of decrease as  $\text{Ri}_b \rightarrow \infty$ .

## 3. Marginal linear stability

### 3.1. Formulation

To investigate the conditions that can support the formation of staircases, we linearise the system (2.8) around linear profiles of buoyancy and velocity with constant shear and buoyancy frequency. We assume that the shear and buoyancy fields can be decomposed as follows, in dimensional form:

$$S = \frac{U}{L} + S', \quad N^2 = \bar{N}^2 + N'^2 \Rightarrow \text{Ri} = \text{Ri}_b + \text{Ri}', \quad (3.1)$$

where the perturbations  $S'$  and  $N'^2$  are small compared to the background states  $U/L$  and  $\bar{N}^2$  respectively and  $\text{Ri}' = \text{Ri}_b \left[ -2\frac{S'}{U/L} + \frac{N'^2}{\bar{N}^2} \right]$ . In dimensionless form, the above becomes:

$$\hat{S} = 1 + \hat{S}', \quad N^2 = 1 + \hat{N}'^2 \Rightarrow \hat{\text{Ri}} = 1 + \hat{\text{Ri}}', \quad (3.2)$$



where  $\hat{S}' \ll 1$ ,  $\hat{N}'^2 \ll 1$  and  $\hat{\text{Ri}}' = -2\hat{S}' + \hat{N}'^2$ . Considering the dimensionless system, removing the hats for clarity and considering a constant dissipation rate of turbulent kinetic energy (set to 1, consistently with  $\hat{\epsilon} = O(1)$  as mentioned above), we obtain, at first order:

$$\begin{cases} \partial_t N'^2 = \frac{1}{\text{Pr}_m \text{Re}} \partial_{zz} N'^2 + \frac{1}{\text{Ri}_b} \partial_{zz} [\text{Ri}' \text{Ri}_b \Gamma'(\text{Ri}_b)], \\ \partial_t S' = \frac{1}{\text{Re}} \partial_{zz} S' + \frac{\text{Pr}_T}{\text{Ri}_b} \partial_{zz} [\text{Ri}' \text{Ri}_b \Gamma'(\text{Ri}_b) - S' \Gamma(\text{Ri}_b) - \text{Ri}' \Gamma(\text{Ri}_b)], \end{cases} \quad (3.3)$$

with  $\text{Ri}' = -2S' + N'^2$ . We now seek normal mode solutions of the form  $[S', N'^2] = [\tilde{S}, \tilde{N}^2] e^{ikz - i\omega t}$  and obtain a system of linear equations for the eigenvectors  $[\tilde{S}, \tilde{N}^2]$ . Since we are interested in non-trivial solutions, we require the determinant of this system to be zero. This condition is equivalent to the dispersion relation:

$$\alpha(k)\omega^2 - i\beta(k)\omega + \gamma(k) = 0, \quad (3.4)$$

where:

$$\begin{cases} \alpha(k) = 1, \\ \beta(k) = f(\text{Ri}_b, \text{Pr}_T, \text{Pr}_m, \text{Re}) k^2, \\ \gamma(k) = C(\text{Ri}_b, \text{Pr}_T, \text{Pr}_m, \text{Re}) k^4, \end{cases} \quad (3.5)$$

with:

$$\begin{cases} f(\text{Ri}_b, \text{Pr}_T, \text{Pr}_m, \text{Re}) = (2\text{Pr}_T - 1)\Gamma'(\text{Ri}_b) - \text{Pr}_T \frac{\Gamma(\text{Ri}_b)}{\text{Ri}_b} - \frac{1}{\text{Re}} \left(1 + \frac{1}{\text{Pr}_m}\right), \\ C(\text{Ri}_b, \text{Pr}_T, \text{Pr}_m, \text{Re}) = \text{Pr}_T \frac{\Gamma(\text{Ri}_b)\Gamma'(\text{Ri}_b)}{\text{Ri}_b} + \frac{\text{Pr}_T}{\text{Pr}_m \text{Re}} \left[ -\frac{\Gamma(\text{Ri}_b)}{\text{Ri}_b} + 2\Gamma'(\text{Ri}_b) \right] \\ \quad - \frac{\Gamma'(\text{Ri}_b)}{\text{Re}} - \frac{1}{\text{Pr}_m \text{Re}^2}. \end{cases} \quad (3.6)$$

A wavenumber  $k$  is thus unstable if the dispersion relation (3.4) admits a solution for frequency  $\omega$  with strictly positive imaginary part. This is equivalent to  $\gamma(k) > 0$  or  $\gamma(k) \leq 0$  and  $\beta(k) > 0$ . These conditions are equivalent to  $f > 0$  or  $C > 0$  and the set of parameters prone to linear instability are therefore:

$$\{(\text{Ri}_b, \text{Pr}_T, \text{Pr}_m, \text{Re}), f > 0\} \cup \{(\text{Ri}_b, \text{Pr}_T, \text{Pr}_m, \text{Re}), C > 0\}. \quad (3.7)$$

The boundary of this set separates linearly unstable and stable parameter regions.

### 3.2. Link with diffusion

The linearised system (3.3) can be written in the matrix form:

$$\begin{bmatrix} \partial_t N'^2 \\ \partial_t S' \end{bmatrix} = \mathbf{D} \begin{bmatrix} \partial_{zz} N'^2 \\ \partial_{zz} S' \end{bmatrix}, \quad (3.8)$$

where:

$$\mathbf{D} = \begin{bmatrix} \Gamma'(\text{Ri}_b) + \frac{1}{\text{Pr}_m \text{Re}} & -2\Gamma'(\text{Ri}_b) \\ \frac{\text{Pr}_T}{\text{Ri}_b} [\text{Ri}_b \Gamma'(\text{Ri}_b) - \Gamma(\text{Ri}_b)] & \frac{\text{Pr}_T}{\text{Ri}_b} [-2\text{Ri}_b \Gamma'(\text{Ri}_b) + \Gamma(\text{Ri}_b)] + \frac{1}{\text{Re}} \end{bmatrix}. \quad (3.9)$$

The matrix  $\mathbf{D}$  may thus be thought of as a diffusion matrix and the real part of its eigenvalues can be interpreted as effective eddy diffusivities of our problem. The trace of this matrix is  $-f$  and its determinant is  $-C$ . Therefore, the instability conditions derived in the previous section are equivalent to the existence of an eigenvalue of this matrix with negative real part and hence an antidiffusive dynamical behaviour that sharpens density gradients. This result can be generalised to the full (nonlinear) system (2.8) (as discussed in more detail

in appendix A) but for the purpose of the stability analysis the above (zero-th order) eddy diffusivities suffice to understand the mechanism at hand.

### 3.3. Dependence on the parameters

In general, the qualitative stability properties do not depend on the particular functional form of the parameterisation  $\Gamma(\text{Ri}_b)$  but rather on  $d\Gamma/d\text{Ri}_b$ . For sufficiently small  $\text{Ri}_b$  such that  $d\Gamma/d\text{Ri}_b > 0$ , (i.e. on the ‘left flank’ of the flux coefficient curve) the system is linearly unstable for sufficiently large values of  $\text{Pr}_T$ . The critical value  $\text{Pr}_{T,c}$  can be very small. For example, instability occurs for  $\text{Pr}_T > \text{Pr}_{T,c} \simeq 0.001$  for flows where  $\Gamma(\text{Ri}_b) \propto \text{Ri}_b$ . As shown in figures 1 and 2,  $\text{Pr}_{T,c}$  appears to be largely insensitive to changes in  $\text{Pr}_m$  and also tends towards zero as  $\text{Re} \rightarrow \infty$ , although it is important to appreciate that the specific case  $\text{Pr}_T = 0$  (that yields  $f < 0$  and  $C \geq 0$ ) is always linearly stable for flows on the increasing left flank of the flux coefficient curve.

Conversely, on the ‘right’ flank where  $d\Gamma/d\text{Ri}_b < 0$ , for all  $\text{Ri}_b > \text{Ri}_b^*$  (i.e. the value of  $\text{Ri}_b$  corresponding to the maximum of the  $\Gamma$ -curve), the flow is always linearly stable for sufficiently large  $\text{Pr}_T$ . For finite values of  $\text{Re}$  (i.e.  $\nu_m \neq 0$ ) and parameterisations of the form (2.11), the critical value  $\text{Pr}_T^c$  for instability depends only on the molecular Prandtl number  $\text{Pr}_m$ , as shown in figure 1. Indeed, if  $\Gamma \propto 1/\text{Ri}_b^p$  the mapping:

$$\text{Ri}_b \rightarrow a\text{Ri}_b, \text{Re} \rightarrow a^{p+1}\text{Re}, \text{Pr}_T \rightarrow \text{Pr}_T, \text{Pr}_m \rightarrow \text{Pr}_m, \quad (3.10)$$

maps  $f \rightarrow 1/a^{p+1}f$  and  $C \rightarrow 1/a^{2p+2}C$ , and so crucially does not affect the sign of these functions (and hence the associated stability properties). Hence, changing  $\text{Re}$  only stretches the boundary between linearly unstable and stable regions in the  $\text{Ri}_b$  direction, as depicted in figure 2. For  $p = 1/2$  (Turner 1968) and  $\text{Pr}_m = 7$  (the typical value of  $\text{Pr}_m$  for thermally-stratified water),  $\text{Pr}_T^c \simeq 0.5$  whereas for  $\text{Pr}_m = 700$  (i.e. water where salinity is the stratifying agent),  $\text{Pr}_T^c \simeq 40$ . The critical value  $\text{Pr}_T^c$  increases with  $\text{Pr}_m$ , consistently with the fact that layering is favoured at large molecular Prandtl number (Taylor & Zhou 2017). (We discuss the strictly inviscid limit  $\nu_m = 0$  (i.e.  $\text{Re} = \infty$ ) in section 3.4.)

The variation of the parameter  $A$  in (2.11) does not significantly affect the stability properties. This can be established through consideration of the mapping:

$$\Gamma \rightarrow a\Gamma, \text{Ri}_b \rightarrow \text{Ri}_b, \text{Re} \rightarrow 1/a\text{Re}, \text{Pr}_T \rightarrow \text{Pr}_T, \text{Pr}_m \rightarrow \text{Pr}_m, \quad (3.11)$$

which maps  $f \rightarrow af$  and  $C \rightarrow a^2C$  which once again does not affect the sign of  $f$  and  $C$ , key to the stability properties. Moreover, we have seen previously that scaling  $\text{Re}$  is equivalent to stretching the marginal stability curves in the  $\text{Ri}_b$  direction only. Therefore, the critical value of  $\text{Pr}_T$  above which no instability is possible does not depend on  $A$  but only on the decreasing power law  $p$  (variation of  $B$  in (2.11) translates the marginal curves in the  $\text{Ri}_b$  direction since this parameter only affects the value  $\text{Ri}_b^*$  of  $\text{Ri}_b$  that maximizes  $\Gamma$ ), suggesting some robustness of our results with respect to the parameterisation of the flux coefficient. More precisely, for given values of  $\text{Pr}_m$  and  $\text{Re}$ , the critical value of  $\text{Pr}_T$  increases with  $p$ . For example, for  $\text{Pr}_m = 7$  and  $\text{Re} = 1000$ , the critical value increases from  $\text{Pr}_T^c \simeq 0.5$  when  $p = 1/2$  to  $\text{Pr}_T^c \simeq 2$  for  $p = 8$ , as shown in figure 3. Note that if  $\Gamma$  saturates at a constant value instead of monotonically decreasing to zero at large bulk Richardson number, then  $\Gamma'(\text{Ri}_b) = 0$  for  $\text{Ri}_b$  large enough and both  $f$  and  $C$  become negative. Then the system is linearly stable for all  $\text{Pr}_T$  and  $\text{Pr}_T^c = 0$ .

All these various results can be summarised as follows. On the decreasing right flank of  $\Gamma$  (i.e. for  $\text{Ri}_b \geq \text{Ri}_b^*$ ) there exists a limit turbulent Prandtl numbers  $\text{Pr}_T^c$  above which no instability is possible and this value depends only on  $\text{Pr}_m$  and  $p$ . For relevant oceanic parameters, this critical value is found to be around  $\text{Pr}_T^c \simeq 0.5 - 0.7$ . Note that this key



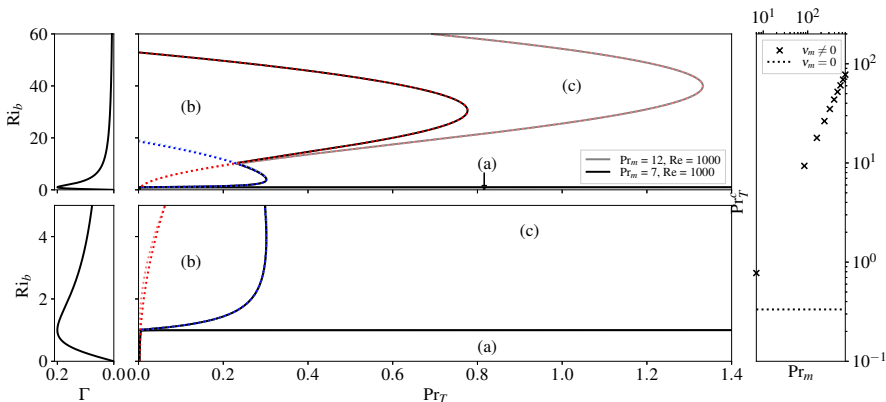


Figure 1: Range of bulk Richardson numbers  $Ri_b$  and turbulent Prandtl numbers  $Pr_T$  prone to layer formation for flows with various molecular Prandtl numbers  $Pr_m$  and  $Re = 1000$ , using parameterisation (2.11) of  $\Gamma$  with  $p = 1$  (depicted in the left panel). Parameters in region (a) and (b) exhibit staircase formation dynamics whereas parameters in region (c) do not. The horizontal boundary between (a) and (c) corresponds to  $Ri_b = Ri_b^*$  (i.e. the bulk Richardson number at which  $\Gamma$  is maximised). The dotted blue curves correspond to the marginal condition  $f = 0$  whereas the dotted red curves correspond to the condition  $C = 0$  as defined in (3.6). The critical turbulent Prandtl number  $Pr_T^c$  above which no instability is possible on the decreasing right flank of the  $\Gamma$ -curve is depicted on the right panel as a function of  $Pr_m$  for  $\nu_m \neq 0$  (i.e. finite values of  $Re$ ) and  $\nu_m = 0$  (i.e.  $Re \rightarrow \infty$ ). From the scaling (3.10), for  $\nu_m \neq 0$ ,  $Pr_T^c$  does not depend on  $Re$ , while for  $\nu_m = 0$   $Pr_T^c$  does not depend on  $Pr_m$ .

result concerning the critical turbulent Prandtl number does not depend on the scaling for the dissipation rate of turbulent kinetic energy. Indeed, for the intermediate scaling presented in section 2.2.2 leading to system (2.9), the associated mapping does not change  $Pr_T^c$  on the right flank of the  $\Gamma$ -curve, but rather only stretches the stability region in the  $Ri_b$  direction as shown in figure 4. Similarly, for the strongly stratified scaling presented in section 2.2.3 leading to system (2.10), the associated mapping again does not change  $Pr_T^c$ , but rather stretches the stability region in the  $Ri_b$  direction and modifies the magnitude of the (unstable) growth rates.

We can also define a critical bulk Richardson number  $Ri_b^c$  above which no instability is possible. For parameterisations with  $\Gamma \propto 1/Ri_b^p$ ,  $Ri_b^c = O(Pr_m Re)^{\frac{1}{p+1}}$  under the assumption that the dissipation rate exhibits inertial scaling. When the dissipation rate exhibits the buoyancy scaling presented in sections 2.2.2 and 2.2.3,  $Ri_b^c = O(Pr_m Re)^{\frac{1}{p+1/2}}$ . The fact that this limit increases with  $Re$  seems reasonable, while the fact that  $Ri_b^c$  increases as  $Pr_m$  is consistent with previous studies establishing that layering seems to be favoured for large molecular Prandtl numbers (Taylor & Zhou 2017).

### 3.4. Limit cases

In this section we analyse four limits of our problem, namely  $\nu_m = 0$ ,  $\bar{N}^2 = 0$ ,  $Pr_T = 0$  and the case  $Pr_m \ll 1$ ,  $Pr_m Re \ll 1$ .

#### 3.4.1. Case $\nu_m = 0$

We first consider the inviscid limit  $\nu_m = 0$  (i.e.  $Re = \infty$ ). On the increasing left flank of the  $\Gamma$ -curve, we have  $C > 0$  for all  $Pr_T > 0$  and therefore the system is unstable in this case (the case  $Pr_T = 0$  gives  $C = 0$  and  $f < 0$  and is therefore stable). Conversely, on the

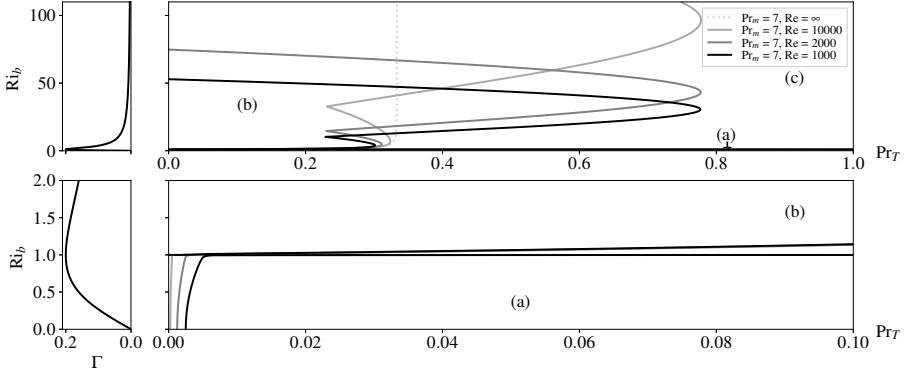


Figure 2: Range of bulk Richardson numbers  $Ri_b$  and turbulent Prandtl numbers  $Pr_T$  prone to layer formation for various Reynolds numbers  $Re$  and  $Pr_m = 7$ , using parameterisation (2.11) of  $\Gamma$  with  $p = 1$  (depicted in the left panel). For  $Re = \infty$  (i.e.  $\nu_m = 0$ ) the boundary between (b) and (c) tends towards the vertical line  $Pr_T = 1/3$ . As suggested by the scaling (3.10), the critical turbulent Prandtl number  $Pr_T^c$  above which no instability is possible on the decreasing right flank of the  $\Gamma$ -curve appears to be independent of  $Re$  for  $\nu_m \neq 0$ .

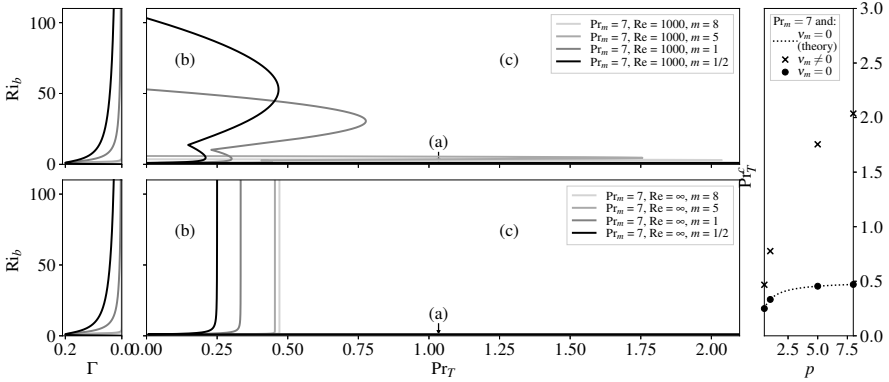


Figure 3: (Top) Range of bulk Richardson numbers  $Ri_b$  and turbulent Prandtl numbers  $Pr_T$  prone to layer formation for  $Pr_m = 7$  and  $Re = 1000$ , using parameterisation (2.11) of  $\Gamma$  with various power laws  $p$  (depicted in the left panel). (Bottom) Same with  $Re = \infty$ . Note that the behaviour of  $\Gamma$  at small  $Ri_b$  is independent of  $p$ . Hence, region (a) is similar to the one depicted in figure 1. (Right) The critical turbulent Prandtl number  $Pr_T^c$  above which no instability is possible on the decreasing right flank of the  $\Gamma$ -curve is depicted on the right panel as a function of  $p$  for  $Pr_m = 7$  and  $\nu_m \neq 0$  (in this case,  $Pr_T^c$  depends on  $Pr_m$  but not on  $Re$ ) and  $\nu_m = 0$ . When  $\nu_m = 0$ ,  $Pr_T^c = p/(2p + 1)$ , as shown by a grey dotted line on the right panel.

decreasing right flank of the  $\Gamma$ -curve, the condition  $C \geq 0$  is no longer well-defined, as is apparent from the definition (3.6). Moreover, the condition  $f \geq 0$  cannot be satisfied on the decreasing right flank of the  $\Gamma$ -curve for  $Pr_T \geq 1/2$ . Hence, on the decreasing right flank of the  $\Gamma$ -curve and for  $\nu_m = 0$ , if  $Pr_T \geq 1/2$  the system is linearly stable and this result is valid for any decreasing  $\Gamma$ -curve, a result first derived by (Kranenburg 1980). For  $\Gamma \propto 1/Ri_b^p$ , this bound can be sharpened to  $Pr_T \geq p/(2p + 1)$ , as shown in figure 3. (This result is

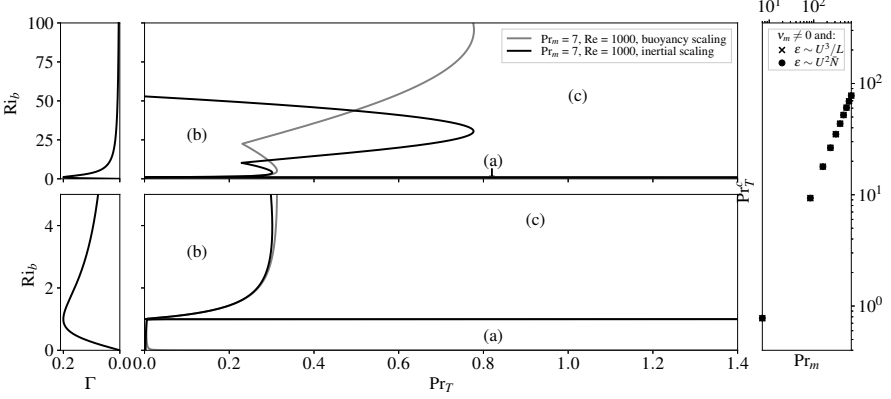


Figure 4: Range of bulk Richardson numbers  $\text{Ri}_b$  and turbulent Prandtl numbers  $\text{Pr}_T$  prone to layer formation for  $\text{Pr}_m = 7$  and  $\text{Re} = 1000$ , using parameterisation (2.11) of  $\Gamma$  with  $p = 1$  (depicted in the left panel) for the different scalings discussed in section 2. The critical turbulent Prandtl number  $\text{Pr}_T^c$  above which no instability is possible on the decreasing right flank of the  $\Gamma$ -curve is depicted on the right panel as a function of  $\text{Pr}_m$  and does not depend on the considered scaling or on  $\text{Re}$  (see scaling (3.10)).

not in contradiction with the critical value  $\text{Pr}_T^c$  for instability found in section 3.3 using the scaling (3.10) since this scaling is valid for finite values of the Reynolds number  $\text{Re}$  only. )

### 3.4.2. Case $\bar{N}^2 = 0$

In the unstratified limit  $\bar{N}^2 = 0$  there is (of course) no buoyancy to mix. The above analysis suggests that the case  $\bar{N}^2 = 0$  (which is equivalent to  $\text{Ri}_b = 0$ ) is linearly unstable (at least for large enough turbulent Prandtl number) and we therefore expect staircase formation in the velocity field rather than in the buoyancy field. Since the scaling presented in section 2.2 cannot be used when  $\bar{N}^2 = 0$ , we consider here the dimensional system (2.6). Let us first linearise the system (2.6) around a state of zero stratification, i.e. we decompose the buoyancy field as  $N^2 = 0 + N'^2$ , implying the decomposition  $\text{Ri} = 0 + N'^2/S^2$  for the Richardson number. We then obtain, at first order:

$$\begin{cases} \partial_t N'^2 = \kappa_m \partial_{zz} N'^2 + \Gamma'(0) \partial_{zz} \left[ \epsilon \frac{N'^2}{S^2} \right], \\ \partial_t S = \nu_m \partial_{zz} S + \text{Pr}_T \Gamma'(0) \partial_{zz} [\epsilon/S]. \end{cases} \quad (3.12)$$

The  $N'^2$ -equation is parabolic, and using a maximum principle (assuming, for example, Dirichlet boundary conditions), we can show that the perturbation  $N'^2$  will remain at all times bounded by the initial perturbation  $\max_z |N'^2(t=0)|$ . Therefore, starting from a perturbation of the buoyancy profile small enough such that the above linearisation stands, this perturbation will remain small and any interesting dynamics will develop in the velocity profile alone.

### 3.4.3. Case $\text{Pr}_T = 0$

In the limit of small turbulent Prandtl numbers, any layering dynamics will occur preferentially in the buoyancy field. More precisely, setting  $\text{Pr}_T = 0$  (and  $\hat{\epsilon} = 1$  for clarity) in (2.8) yields:

$$\begin{cases} \partial_t \hat{N}^2 = \frac{1}{\text{Pr}_m \text{Re}} \partial_{zz} \hat{N}^2 + \frac{1}{\text{Ri}_b} \partial_{zz} [\Gamma(\text{Ri}_b \hat{\text{Ri}})], \\ \partial_t \hat{S} = \frac{1}{\text{Re}} \partial_{zz} \hat{S}, \end{cases} \quad (3.13)$$

and the system is now decoupled. The second equation is a purely diffusive equation that will damp any perturbation in the shear profile exponentially fast on molecular time-scales. Hence, the shear  $\hat{S}$  will tend towards the constant profile  $\hat{S}_0 = 1$ , remembering that this system is dimensionless. The  $\hat{N}^2$ -equation is prone to the Phillips mechanism, as layers will form in the buoyancy profile when the right-hand side  $F(\hat{N}^2) = \frac{1}{\text{Pr}_m \text{Re}} \hat{N}^2 + \frac{1}{\text{Ri}_b} \Gamma \left( \text{Ri}_b \frac{\hat{N}^2}{\hat{S}_0} \right)$  is a decreasing function of  $\hat{N}^2$ , (i.e. on the ‘right flank’) whereas any perturbation will be damped on the increasing ‘left’ flank of this function. This observation is consistent with linear stability analysis. Indeed, for  $\text{Pr}_T = 0$  we obtain the equivalent condition for instability:

$$f \geq 0 \text{ or } C \geq 0 \Leftrightarrow C \geq 0 \Leftrightarrow \frac{1}{\text{Pr}_m \text{Re}} + \Gamma'(\text{Ri}_b) \leq 0. \quad (3.14)$$

Therefore, the case  $\text{Pr}_T = 0$  is equivalent to the Phillips mechanism as formulated in (Phillips 1972) and in this limit the system is linearly stable for  $\text{Ri}_b \leq \text{Ri}_b^*$  and layering can only happen for sufficiently stratified flows. If we assume that  $\Gamma'(\text{Ri}_b) \rightarrow 0$  as  $\text{Ri}_b \rightarrow \infty$ , there exists another critical value of the bulk Richardson number  $\text{Ri}_b^c \geq \text{Ri}_b^*$  such that the system is linearly stable for  $\text{Ri}_b \geq \text{Ri}_b^c$ . This critical value, defined by the condition  $\Gamma'(\text{Ri}_b) = -1/\text{Pr}_m \text{Re}$  (see equation 3.14), is an increasing function of  $\text{Re}$  and goes to infinity as  $\text{Re} \rightarrow \infty$ . This is consistent with the fact that viscous effects are expected to inhibit perturbation growth. As shown in section 3.3, this result can be extended to  $\text{Pr}_T \ll 1$ . On the contrary, for larger value of  $\text{Pr}_T$ , the instability seems to be favoured for small bulk Richardson numbers (see section 3.3) i.e. sufficiently weakly stratified flows. Hence, once again the central conclusion is that in the presence of shear and buoyancy driven turbulence, the Phillips mechanism seems to survive only in the limit of small turbulent Prandtl numbers.

#### 3.4.4. Case $\text{Pr}_m \ll 1$ , $\text{Pr}_m \text{Re} \ll 1$

Let us consider the case of small molecular Prandtl and Péclet numbers, where the Péclet number is defined as  $\text{Pe} := \text{Pr}_m \text{Re}$  and can be understood as the ratio of the advective and diffusive time-scales. This case is relevant to astrophysical stratified turbulent flows where  $\text{Pr}_m$  usually ranges between  $10^{-9}$  and  $10^{-5}$  and can therefore sustain small  $\text{Pe}$ , high  $\text{Re}$  regimes (Garaud *et al.* 2015). In the limit  $\text{Pr}_m \ll 1$  and  $\text{Pe} \ll 1$  (and considering finite Reynolds, bulk Richardson and turbulent Prandtl numbers), consideration of (3.6) shows that  $f \rightarrow -\infty$ , while  $C \rightarrow \infty$  for  $\text{Pr}_T \left[ -\frac{\Gamma(\text{Ri}_b)}{\text{Ri}_b} + 2\Gamma'(\text{Ri}_b) \right] - \frac{1}{\text{Re}} > 0$  and  $C \rightarrow -\infty$  otherwise. Therefore on the decreasing right flank of the  $\Gamma$ -curve (i.e. where  $\Gamma'(\text{Ri}_b) \leq 0$ ), both  $f$  and  $C$  are negative and the system is linearly stable. Hence, for sufficiently large  $\text{Ri}_b$ , layering is prohibited, consistently with the fact that buoyancy anomalies are rapidly diffused for  $\text{Pe} \ll 1$  (Cope *et al.* 2020).

## 4. Instability properties

### 4.1. Wavenumber dependence

The dispersion relation (3.4) yields:

$$\omega = \frac{1}{2} \left[ i k^2 f \pm \Delta_0(k)^{1/2} \right], \quad (4.1)$$

where  $\Delta_0(k) := (-i\beta)^2 - 4\alpha\gamma = -k^4 f^2 - 4k^4 C \propto k^4$ . Therefore  $\omega \propto k^2$  and any perturbation of linearly unstable velocity and buoyancy profiles will grow with growth rates that are proportional to the square of the vertical wavenumber, as shown in figure 5. Hence, the model exhibits an ‘ultraviolet catastrophe’ of unbounded growth at small scales. This unphysical

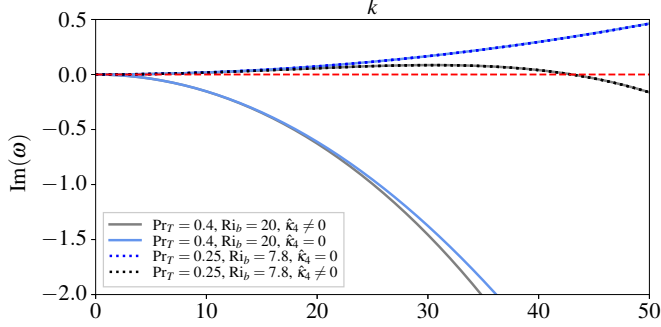


Figure 5: Growth rate as a function of the wavenumber  $k$  for various sets of parameters and with or without hyperdiffusion  $\hat{\kappa}_4$ .

behaviour is a consequence of the fact that flux-gradient parameterisations of eddy turbulent fluxes inevitably break down at small scales (namely scales below the representative scale of the turbulent microstructures that shape the flow on larger scales). Similar issues have been encountered in the double-diffusion literature. For example, Radko (2014) shows that fingering flux-gradient models tend to fail ‘when the size of the phenomenon of interest is comparable to the scale of microstructure which those laws strive to parameterize’.

Furthermore, Ma & Peltier (2021) encounter an ultraviolet catastrophe when studying salt-fingering-engendered thermohaline staircases using a diffusive parameterisation of heat and salinity turbulent fluxes. Again, the problem originates from the assumption that gradient-flux laws are valid at all scales, even those that are smaller than salt-finger widths. To resolve the problem, hyperdiffusive terms were added to the model to correct the model and dampen perturbations at small scales. This can be justified by a multiscale analysis of the problem (as performed by Radko (2019)) that takes into account the interaction between small (microstructure turbulence) and larger scales.

#### 4.2. Regularisation of the model at small scales

Following the ideas of Radko (2019) and Ma & Peltier (2021), we add hyperdiffusion terms to regularise our dimensionless system (2.8) as follows:

$$\begin{cases} \partial_t \hat{N}^2 = \frac{1}{\text{Pr}_m \text{Re}} \partial_{zz} \hat{N}^2 + \frac{1}{\text{Ri}_b} \partial_{zz} [\Gamma(\text{Ri}_b \hat{\text{Ri}}) \hat{\epsilon}] - \hat{\kappa}_4 \partial_z^4 \hat{N}^2, \\ \partial_t \hat{S} = \frac{1}{\text{Re}} \partial_{zz} \hat{S} + \frac{\text{Pr}_T}{\text{Ri}_b} \partial_{zz} \left[ \frac{\Gamma(\text{Ri}_b \hat{\text{Ri}}) \hat{\epsilon}}{\hat{S} \hat{\text{Ri}}} \right] - \hat{\kappa}_4 \partial_z^4 \hat{S}, \end{cases} \quad (4.2)$$

where the scaling factor  $\hat{\kappa}_4$  will be chosen later.

Importantly, the addition of hyperdiffusion does not change our stability results. Following the same approach as in section 3, it can be shown that the dispersion relation becomes:

$$\alpha_h(k) \omega^2 - i \beta_h(k) \omega + \gamma_h(k) = 0, \quad (4.3)$$

where:

$$\begin{cases} \alpha_h(k) = 1, \\ \beta_h(k) = -2\hat{\kappa}_4 k^4 + k^2 f(\text{Ri}_b, \text{Pr}_T, \text{Pr}_m, \text{Re}), \\ \gamma_h(k) = k^4 [-\hat{\kappa}_4^2 k^4 + \hat{\kappa}_4 f(\text{Ri}_b, \text{Pr}_T, \text{Pr}_m, \text{Re}) k^2 + C(\text{Ri}_b, \text{Pr}_T, \text{Pr}_m, \text{Re})], \end{cases} \quad (4.4)$$

where  $f$  and  $C$  are identical to the previous expressions given in (3.6). A wavenumber  $k$  is unstable if  $\gamma_h(k) > 0$  or  $\gamma_h(k) \leq 0$  and  $\beta_h(k) > 0$ . The condition  $\beta_h(k) > 0$  is equivalent

to:

$$k^2 < f/2\hat{\kappa}_4. \quad (4.5)$$

Therefore the existence of  $k \geq 0$  such that  $\beta_h(k) > 0$  is equivalent to  $f > 0$ . Then, if a set of parameters  $(\text{Ri}_b, \text{Pr}_T, \text{Pr}_m, \text{Re})$  satisfy  $f > 0$  we can find small wavenumbers  $k < (f/2\hat{\kappa}_4)^{1/2}$  that are linearly unstable. Using the fact that  $\gamma_h/k^4$  is a polynomial of degree two in  $k^2$ , we can show that the existence of a wavenumber  $k \geq 0$  such that  $\gamma_h(k) > 0$  is equivalent to  $C > 0$  or  $C \leq 0$  and  $f > 0$  and  $f^2 > -4C$ . Combining the above conditions, the unstable set of parameters is defined by  $\{f > 0\} \cup \{C > 0\} \cup [\{C \leq 0\} \cap \{f > 0\} \cap \{f^2 > -4C\}] = \{f > 0\} \cup \{C > 0\}$  and therefore the existence of a linearly unstable wavenumber is equivalent to  $f > 0$  or  $C > 0$ , exactly as in section 3. Moreover, using again the polynomial structure of  $\gamma_h/k^4$ , we can show that the maximum wavenumber satisfying  $\gamma_h(k) \geq 0$  is  $O(\hat{\kappa}_4 \max(f, \sqrt{C})/\hat{\kappa}_4^2)^{1/2} = O(\max(f, \sqrt{C})/\hat{\kappa}_4)^{1/2}$  when it exists. Therefore, since the magnitude of  $f$  and  $\sqrt{C}$  are set by  $1/\text{Re}$  for the range of Reynolds numbers considered here, the maximum unstable wavenumber, if it exists, is  $O(1/\text{Re}\hat{\kappa}_4)^{1/2}$ .

Since  $f$  and  $C$  do not depend on  $\hat{\kappa}_4$ , the boundaries between stable and unstable regions also do not depend on the ‘strength’ of the regularising hyperdiffusion. However,  $\hat{\kappa}_4$  does affect the magnitude of the growth rates (but not their sign), the particular value of the maximum unstable wavenumber ( $O(1/\text{Re}\hat{\kappa}_4)^{1/2}$  as shown previously) as well as the wavenumber associated with the maximum growth rate. Therefore the early-time length scale of the staircases which (potentially) form will depend on the strength of the imposed hyperdiffusion.

Using the above, we can determine a relevant value for  $\hat{\kappa}_4$ . More precisely, it is chosen so that the largest unstable wavenumber is of order or smaller than, in dimensionless form,  $L/L_K$  where  $L_K := (\nu_m^3/\epsilon)^{1/4}$  is the Kolmogorov length scale. We choose this scale as it is the scale below which viscosity finally dissipates kinetic energy. Since the flows we are interested in typically have  $\text{Pr}_m \gtrsim 1$ ,  $L_K > L_B := L_K/\sqrt{\text{Pr}_m}$ , the Batchelor scale at which fine structure in the scalar field is smoothed out by diffusivity. Therefore  $L_K$  is a natural conservative scale to choose to regularise the build-up of perturbations at small scales. We have shown that the largest unstable wavenumber is of order  $(1/\text{Re}\hat{\kappa}_4)^{1/2}$ . Therefore, for  $\text{Re} = O(1000)$ , we want  $\hat{\kappa}_4 \gtrsim 10^{-8}$ . For the purpose of our numerical experiment (section 5) and in order to form layers that are not too small nor too large, we henceforth choose the conservative values  $\hat{\kappa}_4 = 10^{-5}$  or  $10^{-7}$ , depending on the particular choice of the parameters, as discussed further below.

Using the above corrections, the system now has a maximum unstable wavenumber  $k_{\max}$  and a maximum growth rate  $\sigma_{\max}$  attained at  $k_{\max}$  (remembering that if  $k_{\max} = 0$  and  $\sigma_{\max} \leq 0$  then the system is linearly stable). We plot these quantities for various values of the parameters in figures 6 and 7. The maximum growth rate  $\sigma_{\max}$  may be interpreted as a relevant time scale of layer formation whereas  $k_{\max}$  may be thought of as the length scale of the layers potentially forming, at least at early times, before subsequent coarsening through layer merger, as we discuss further below. It is apparent that the unstable region on the decreasing right flank of the  $\Gamma$ -curve (region (b)) divides into two distinct regions of relatively large  $\sigma_{\max}$  separated by a gap of relatively small  $\sigma_{\max}$ , suggesting the existence of different types of unstable dynamics for  $\text{Ri}_b \geq \text{Ri}_b^*$ .

In this situation, the dispersion relation is:

$$\omega = \frac{1}{2} \left[ -2i\hat{\kappa}_4 k^4 + ik^2 f \pm \Delta_h(k)^{1/2} \right], \quad (4.6)$$

where  $\Delta_h(k) := (-i\beta_h)^2 - 4\alpha_h\gamma_h = -k^4 f^2 - 4k^4 C = \Delta_0(k)$  does not depend on  $\hat{\kappa}_4$ . Therefore, if  $\Delta_0(k) > 0$ , the component of vertical wavenumber  $k$  of the solution of the linearised problem will be exponentially increasing or decreasing (depending on the sign of



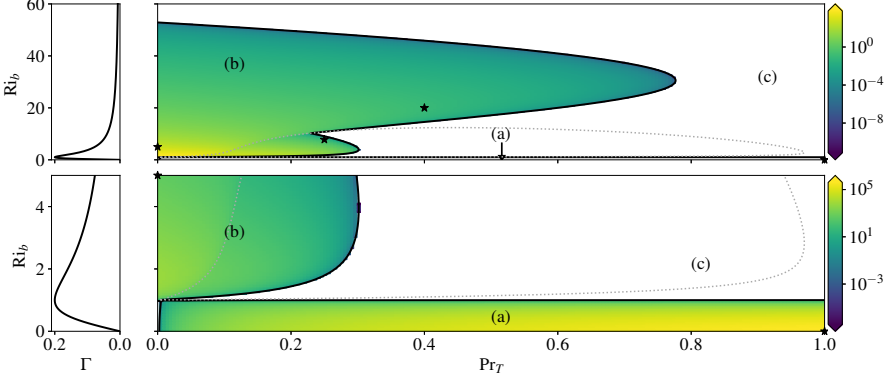


Figure 6: Variation of maximum growth rate  $\sigma_{\max}$  (on a logarithmic scale) with bulk Richardson number  $Ri_b$  and turbulent Prandtl number  $Pr_T$  for  $Pr_m = 7$ ,  $Re = 1000$ ,  $\hat{\kappa}_4 = 10^{-7}$  and a parameterisation of  $\Gamma$  as depicted on the left panels (with  $p = 1$ ). The white regions correspond to  $\sigma_{\max} \leq 0$  and hence linearly stable regions. The black line separates linearly stable and unstable regions (and do not depend on the hyperdiffusion  $\hat{\kappa}_4$ ). The dotted grey line corresponds to the contour line  $\Delta = 0$ . The stars mark the parameter values of the cases studied in section 5. Note from the vertical axes that the lower panels correspond to the small  $Ri_b$  region of the upper panels.

the imaginary part of  $\omega$ ) while oscillating with a frequency  $1/2\Delta_0(k)^{1/2}$ . The sign of  $\Delta_0$  is the sign of  $\Delta := -f^2 - 4C$ , which depends only on the parameters  $Ri_b$ ,  $Pr_T$ ,  $Pr_m$  and  $Re$ , but crucially not on  $k$ . We therefore expect different dynamics depending on the sign of  $\Delta$ : a ‘oscillatory’ behaviour for  $\Delta > 0$ ; and purely damped or exponentially growing for  $\Delta \leq 0$ . Importantly, this result is independent of the addition of an hyperdiffusion correction. The contour line corresponding to  $\Delta = 0$  is plotted on figure 6. Interestingly, it aligns with the gap of small  $\sigma_{\max}$  mentioned above and shown in figure 6. This supports again the fact that at least two different types of unstable dynamics coexist in the unstable region (b).

## 5. Nonlinear dynamics

In this section, we numerically solve the corrected dimensionless system (4.2) and compare the nonlinear dynamics to the linear stability analysis presented above.

In order to solve (4.2), boundary conditions need to be specified. In the following, we consider periodic boundary conditions for the shear  $S$  and stratification  $N^2$ :

$$\forall t \geq 0, S(t, z = 0) = S(t, z = 1), N^2(t, z = 0) = N^2(t, z = 1). \quad (5.1)$$

These conditions quantize the range of admissible vertical wavenumbers  $k$ , which are of the form  $k = 2\pi n$  where  $n = 0, 1, \dots$  (in practice,  $n$  will in fact be bounded above by  $1/dz$  where  $dz$  is the spatial grid size of our numerical calculations). Since the case  $n = 0$  has zero growth rate, if the maximum unstable wavenumber  $k_{\max}$  (which exists thanks to the addition of hyperdiffusion) is smaller than  $2\pi$ , the system will be ‘numerically’ linearly stable, although it could of course have been linearly unstable provided other boundary conditions were chosen. We plot the maximum unstable wavenumber for various values of the parameters in figure 7.

Inspired by the linear stability analysis (section 3) we consider the following dimensionless

initial condition for three different choices with non-zero  $Ri_b$  as marked on figure 7:

$$\forall z \in [0, 1], \quad S(t = 0, z) = 1 + \tilde{n}(z), \quad N^2(t = 0, z) = 1 + \tilde{n}(z), \quad (5.2)$$

where  $\tilde{n}$  is a small random noise, normally distributed with 0 mean and 0.01 standard deviation. For the zero  $Ri_b$  case (case 2),  $\bar{N}^2 = 0$  and we then set  $N^2(t = 0, z) = \max(0, \tilde{n}(z)) \geq 0$  so that the profile is always stably stratified.

Using the above boundary and initial conditions, system (4.2) can be solved using the method presented in appendix B. In order to obtain the velocity and the buoyancy fields from the computed shear and the stratification profiles,  $S$  and  $N^2$  are integrated over space. The integration constants are chosen so that the conservation of mass and momentum is respected:

$$\forall t \geq 0, \quad \int_0^1 b(t, z) dz = \int_0^1 b(0, z) dz, \quad \int_0^1 u(t, z) dz = \int_0^1 u(0, z) dz. \quad (5.3)$$

We focus our attention on four sets of linearly unstable parameters as marked with stars on figure 7:

- **Case 1:**  $Ri_b = 5$  (on the decreasing right flank of the  $\Gamma$ -curve),  $Pr_T = 0$ ,  $Pr_m = 7$  and  $Re = 1000$ . This set of parameters illustrates the theoretical results presented in section 3.4.3 for  $Pr_T = 0$ . We show the numerical solution in figure 8. Perturbations in the velocity profile are damped and the linear velocity profile (constant shear profile) is retrieved whereas perturbations in the buoyancy profile grow and form layers that eventually merge.

- **Case 2:**  $\bar{N}^2 = 0$ ,  $Pr_T = 1$ ,  $Pr_m = 7$  and  $Re = 1000$ . This choice of parameters illustrates the limiting unstratified case  $\bar{N}^2 = 0$  presented in section 3.4.2. We show the numerical results in figure 9. Here the perturbations in the buoyancy profile do not grow above their initial magnitude and layering occurs in the velocity profile.

- **Case 3:**  $Ri_b = 7.8$  (decreasing right flank of the  $\Gamma$ -curve),  $Pr_T = 0.25$ ,  $Pr_m = 7$  and  $Re = 1000$ . This set of parameters has been chosen in the unstable region (b) as shown in figure 7, so that  $\Delta > 0$ . The maximum growth rate is  $\sigma_{\max} \simeq 0.09$  and attained for a wavenumber  $k_{\max} \simeq 30.4$ . Therefore we expect the development of structures of length-scale  $\sim 0.2$  dimensionless space units in around 10 dimensionless time units. Since  $\Delta > 0$ , we also expect some kind of oscillatory behaviour in the time evolution of the buoyancy and velocity profiles. We show the numerical results as well as the evolution in time of the amplitude of the fastest growing mode (corresponding to  $k_{\max}$ ) in figures 10, 11, 12 and 13. After a transient phase, yet before the saturation of the instability, the perturbation appears to grow at the predicted rate simultaneously and concomitantly in both the shear and stratification profiles. Furthermore, the development of buoyancy and velocity staircases appears to be locked and in phase. Interestingly, the layers seem to ‘pulse’ with a period of approximately 3 dimensionless time units, corresponding to the theoretical period  $2\pi/(0.5\Delta_0(k_{\max})^{1/2}) \simeq 3$  (see section 4). The initial layers (before they start merging), have a length scale of  $\sim 0.2$  dimensionless space units, demonstrating the relevance of the linear stability analysis. Similar dynamics is observed for other sets of linearly unstable parameters on the decreasing right flank of the  $\Gamma$ -curve satisfying  $\Delta > 0$ .

- **Case 4:**  $Ri_b = 20$  (also on the decreasing right flank of the  $\Gamma$ -curve),  $Pr_T = 0.4$ ,  $Pr_m = 7$  and  $Re = 1000$ . This set of parameters lies on the linearly unstable region (b) and satisfies  $\Delta \leq 0$ . It has been chosen so that the unstable branch of the growth rate spectrum associated with this case is similar to the one associated with the previous case (see figure 5). Therefore, the relevant time and length scales associated with the development of potential instabilities will be similar in both cases and we expect a structure of length scale  $\sim 0.2$  dimensionless space units to appear. We show the numerical results as well as the time evolution of the amplitude of the fastest growing mode in figures 10, 14, 15 and 16. After a short transient

(and before saturation of the instability), the fastest growing mode again grows at the expected theoretical rate. No oscillations in time are observed, in line with  $\Delta \leq 0$ . Interestingly, and unlike the previous case where the perturbations in the stratification and the shear seemed to evolve concomitantly and layers form almost simultaneously and in phase in the buoyancy and velocity profiles, buoyancy layers seem to form slightly before velocity ones. The initial layers (before they start merging) have a length scale of  $\sim 0.2$  dimensionless space units, once again as predicted by the linear theory. As the instability saturates, layers start to merge. Similar dynamics is observed for other sets of parameters on the decreasing right flank of the  $\Gamma$ -curve satisfying  $\Delta \leq 0$ . This behaviour is also reminiscent of the case  $\text{Pr}_T = 0$  exhibiting the Phillips mechanism and associated with the condition  $C \geq 0$  (that implies  $\Delta \leq 0$ ) where layers form exclusively in the buoyancy field.

All in all, the unstable parameters region should be thought of as being divided into three subregions: a low  $\text{Ri}_b$  region (corresponding to  $\text{Ri}_b \ll 1$ ) where the dynamics is mostly shear-driven and where layer formation happens in the velocity profile since there are no buoyancy gradients to mix; an intermediate  $\text{Ri}_b$  and small  $\text{Pr}_T$  region (corresponding to  $\text{Ri}_b \geq \text{Ri}_b^*$ ,  $\Delta > 0$ ) where the dynamics is buoyancy- and shear-driven and where the layering occurs almost simultaneously in both the buoyancy and velocity fields with layer ‘pulsation’; and an intermediate to large  $\text{Ri}_b$  and small  $\text{Pr}_T$  region (corresponding to  $\text{Ri}_b \geq \text{Ri}_b^*$  and  $\Delta \leq 0$ ) where the dynamics is again shear- and buoyancy-driven but where the layering arises firstly in the buoyancy field and layers merge rather than pulse.

The nonlinear dynamics also pinpoint the qualitatively different mixing happening in the well-mixed layers and in the strongly stratified interfaces separating layers. Inside the layers, the density anomalies are smoothed and mixing can therefore be described by an appropriately defined positive eddy diffusivity (see appendix A). In the interfaces, such an eddy diffusivity becomes formally negative (see figure 8 and 16 for instance) and the mixing is therefore in some sense ‘antidiffusive’, in the specific sense that it appears to sharpen the buoyancy gradients by scouring the interface. Although further analysis and direct numerical simulations are undoubtedly needed, the local maxima of  $\Gamma$  at the borders of the density interfaces points suggests scouring dynamics, as does the observation that inside the interfaces, the flux coefficient is minimal, supporting the hypothesis that these structures are barriers to mixing.

## 6. Discussion

In this paper, we have derived a reduced order model aiming at describing the formation and evolution of density staircases in sheared and (stably) stratified turbulent flows. Following the ideas of Phillips (1972) and Posmentier (1977), we have parameterised the turbulence using flux-gradient models. Using this framework, we have determined regions in the parameter space ( $\text{Ri}_b$ ,  $\text{Pr}_T$ ,  $\text{Pr}_m$ ,  $\text{Re}$ ) prone to layer formation. Crucially, these regions depend on the monotonicity of variation of the flux coefficient  $\Gamma$  with the bulk Richardson number  $\text{Ri}_b$ . Since experimental, observational and numerical evidence seem to indicate that  $\Gamma$  increases with  $\text{Ri}_b$  up to some critical value  $\text{Ri}_b^*$  and plausibly decreases for  $\text{Ri}_b \geq \text{Ri}_b^*$  (Linden 1979, 1980; Wells *et al.* 2010), the staircase ‘instability’ depends on the size of  $\text{Ri}_b$  compared to  $\text{Ri}_b^*$ . We have also presented theoretical evidence that this instability depends on the turbulent Prandtl number  $\text{Pr}_T$ .

On the increasing left flank of the  $\Gamma$ -curve (i.e. its dependence on  $\text{Ri}_b$ ), the instability occurs for  $\text{Pr}_T$  above a (very small) given threshold, found to be around 0.001 for the case with  $\Gamma(\text{Ri}_b) \propto \text{Ri}_b$ ,  $\text{Pr}_m = 7$  and  $\text{Re} = \mathcal{O}(1000)$ . Therefore, for sufficiently small  $\text{Pr}_T \ll 1$ ,  $\text{Ri}_b < \text{Ri}_b^*$  is stable to layer formation, retrieving Phillips result that stratification needs to be sufficiently large (and on the decreasing right flank of the  $\Gamma$ -curve) to be prone to staircase

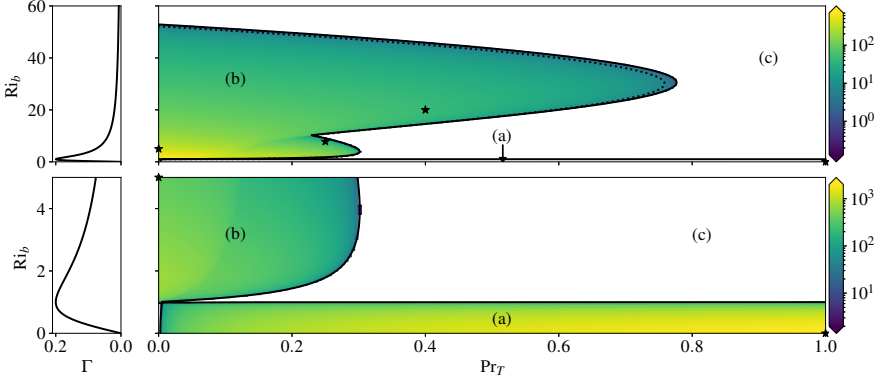


Figure 7: Variation of maximum unstable wavenumber  $k_{\max}$  (in logarithmic scale) with bulk Richardson number  $Ri_b$  and turbulent Prandtl number  $Pr_T$  for  $Pr_m = 7$ ,  $Re = 1000$ ,  $\hat{\kappa}_4 = 10^{-7}$  and a parameterisation of  $\Gamma$  depicted on the left panels (with  $p = 1$ ). The white regions correspond to  $k_{\max} = 0$  and hence linearly stable regions. The black line separates linearly stable and unstable regions. The dotted line corresponds to the  $k_{\max} = 2\pi$  contour line. Whereas parameters in the colored regions (regions (a) and (b)) are prone to layer formation, only parameters in region inside the dotted line will exhibit layering dynamics numerically. The stars correspond to the cases studied in section 5.

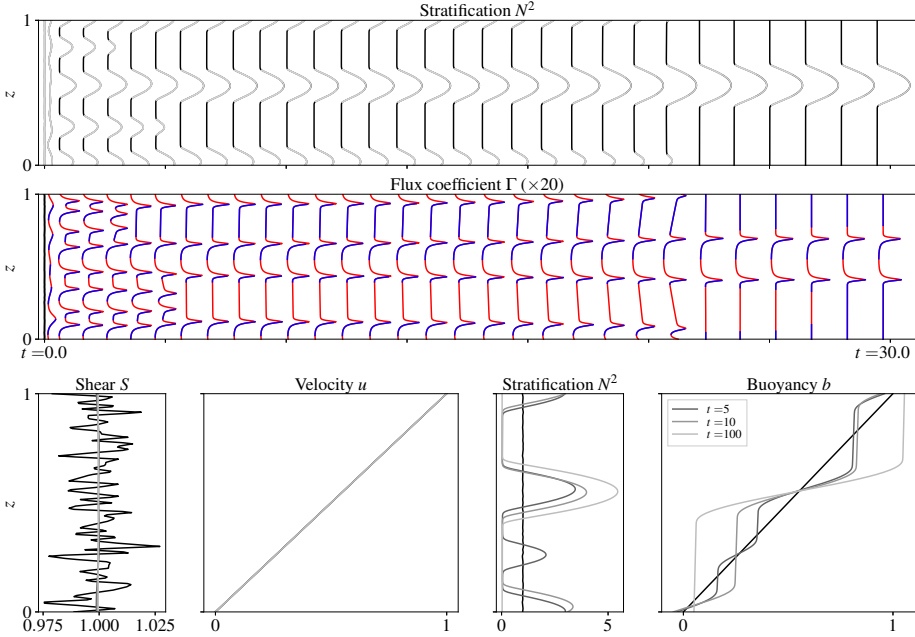


Figure 8: Evolution of the buoyancy and velocity profiles for case 1 with  $Ri_b = 5$ ,  $Pr_T = 0$ ,  $Pr_m = 7$  and  $Re = 1000$ . The black lines correspond to the initially disturbed profiles (the same perturbation is used for both the velocity and buoyancy). On the top two panels, the horizontal axis is time and each profile is separated by one dimensionless time unit. For the buoyancy profiles, the grey regions correspond to regions where the effective eddy diffusivity defined in appendix A is negative. For the flux coefficient profiles, red corresponds to upwelling while blue corresponds to downwelling. (Note that in order to form layers that are big enough to be visible, we use the higher value of  $\hat{\kappa}_4 = 10^{-5}$ .)

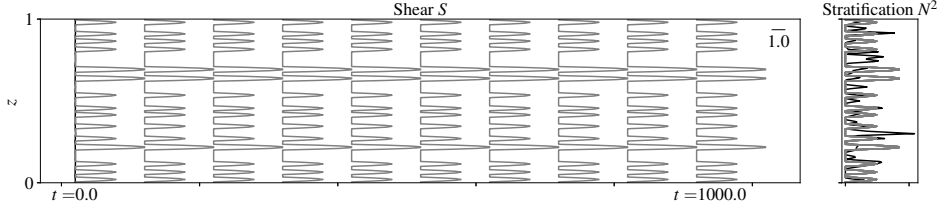


Figure 9: Evolution of the shear and stratification for case 2 with  $\bar{N}^2 = 0$ ,  $\text{Pr}_T = 1$ ,  $\text{Pr}_m = 7$  and  $\text{Re} = 1000$ . On the left panel, the horizontal axis is time and each profile is separated by 100 dimensionless time units. On the right panel, the initial condition (black line) as well as the profile at a later time (grey lines) can be plotted on the same axis, demonstrating that the magnitude of the perturbations on the buoyancy profile do not grow significantly above the initial perturbation. (Note that in order to form layers that are big enough to be visible, we use the higher value of  $\hat{\kappa}_4 = 10^{-5}$ .)

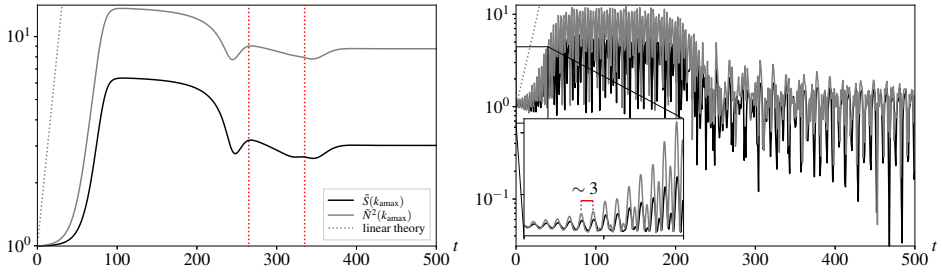


Figure 10: Time evolution of the amplitude of the fastest growing mode (normalized by the initial amplitude) for: case 4 with  $\text{Ri}_b = 20$ ,  $\text{Pr}_T = 0.4$ ,  $\text{Pr}_m = 7$ ,  $\text{Re} = 1000$  and  $\hat{\kappa}_4 = 10^{-7}$  (left panel); and case 3 with  $\text{Ri}_b = 7.8$ ,  $\text{Pr}_T = 0.25$ ,  $\text{Pr}_m = 7$ ,  $\text{Re} = 1000$  and  $\hat{\kappa}_4 = 10^{-7}$  (right panel) for the shear (black line) and the buoyancy (grey line). The dotted grey line corresponds to the evolution predicted by the linear theory. The red dotted lines correspond to the end of merging events.

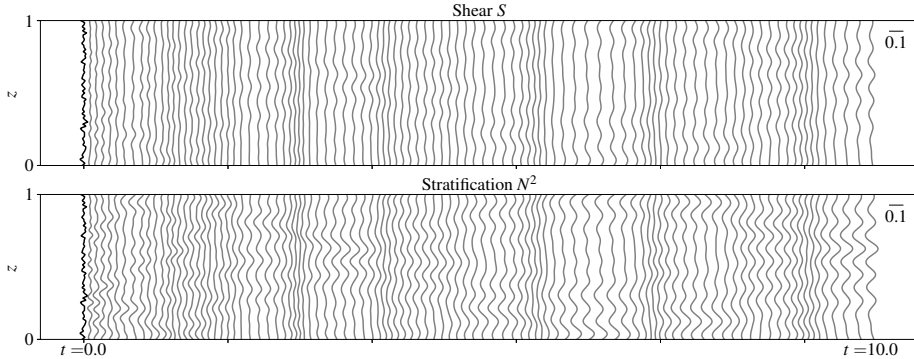


Figure 11: Evolution of the buoyancy and velocity profiles for case 3 with  $\text{Ri}_b = 7.8$ ,  $\text{Pr}_T = 0.25$ ,  $\text{Pr}_m = 7$  and  $\text{Re} = 1000$ . The black lines correspond to the initially disturbed profiles. On the top panel, the horizontal axis is time and each profile is separated by 0.1 dimensionless time unit. We use the lower value of  $\hat{\kappa}_4 = 10^{-7}$ .

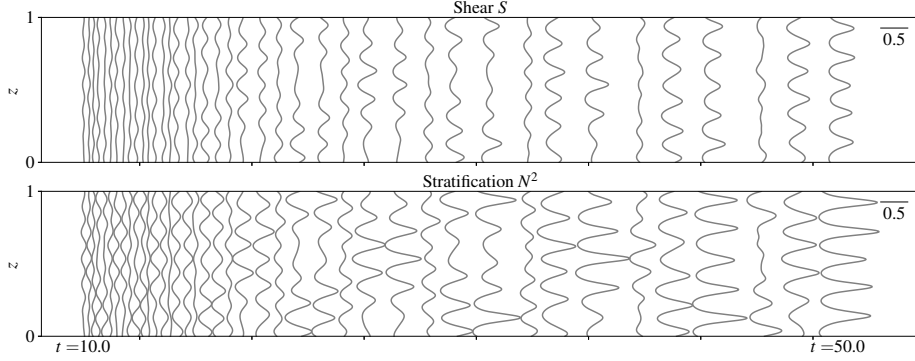


Figure 12: Later time evolution in the same format as figure 11. The horizontal axis is again time and each profile is separated by 1 dimensionless time unit.

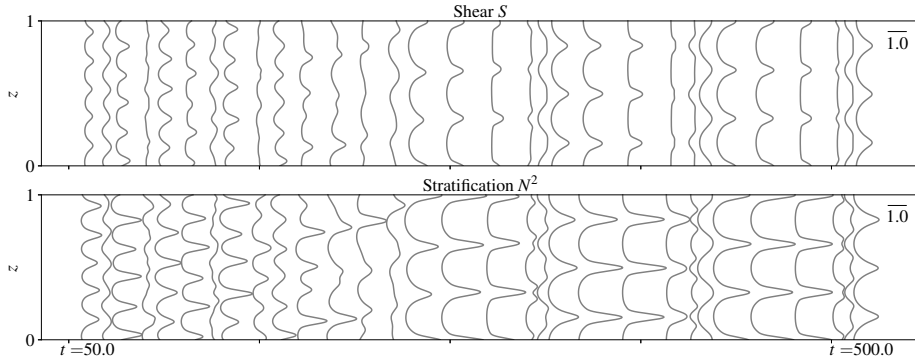


Figure 13: Further later time evolution in the same format as figure 11. The horizontal axis is again time and each profile is separated by 15 dimensionless time unit.

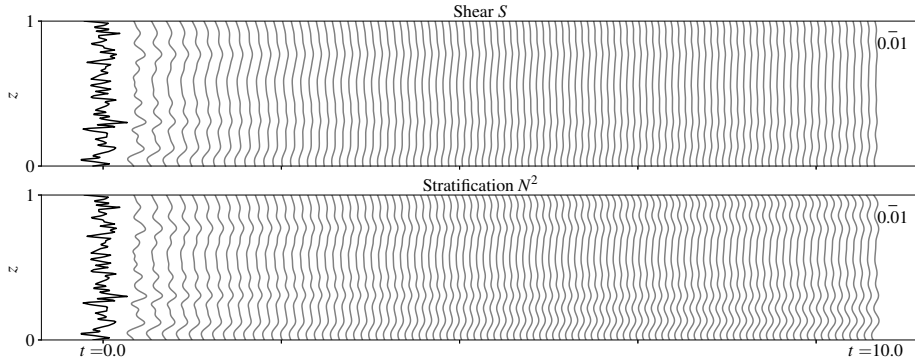


Figure 14: Evolution of the buoyancy and velocity profiles for case 4 with  $Ri_b = 20$ ,  $Pr_T = 0.4$ ,  $Pr_m = 7$  and  $Re = 1000$ . The bold black lines correspond to the initially disturbed profiles. On the top panel, the horizontal axis is time and each profile is separated by 0.1 dimensionless time unit. We use the lower value of  $\hat{\kappa}_4 = 10^{-7}$ .

formation. However, for non-zero (though still small) values of  $Pr_T$  layer instabilities can actually be triggered in weakly stratified flows (in the sense  $Ri_b < Ri_b^*$ ) in the presence of buoyancy and shear driven turbulence.

Conversely, on the decreasing right flank of the  $\Gamma$ -curve, the instability occurs for



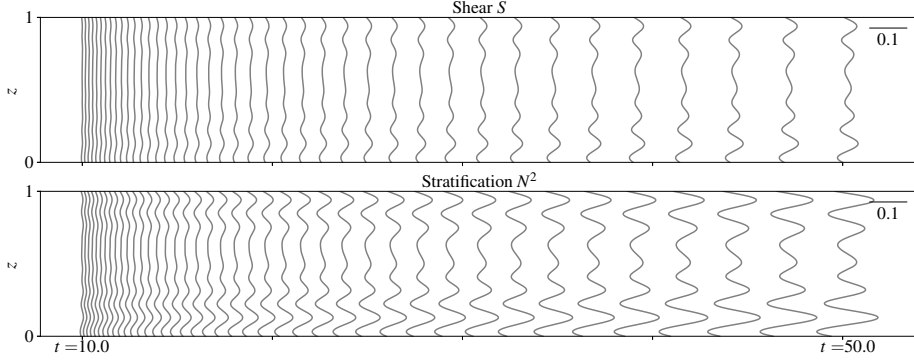


Figure 15: Later time evolution in the same format as figure 14. The horizontal axis is again time and each profile is separated by 1 dimensionless time unit.

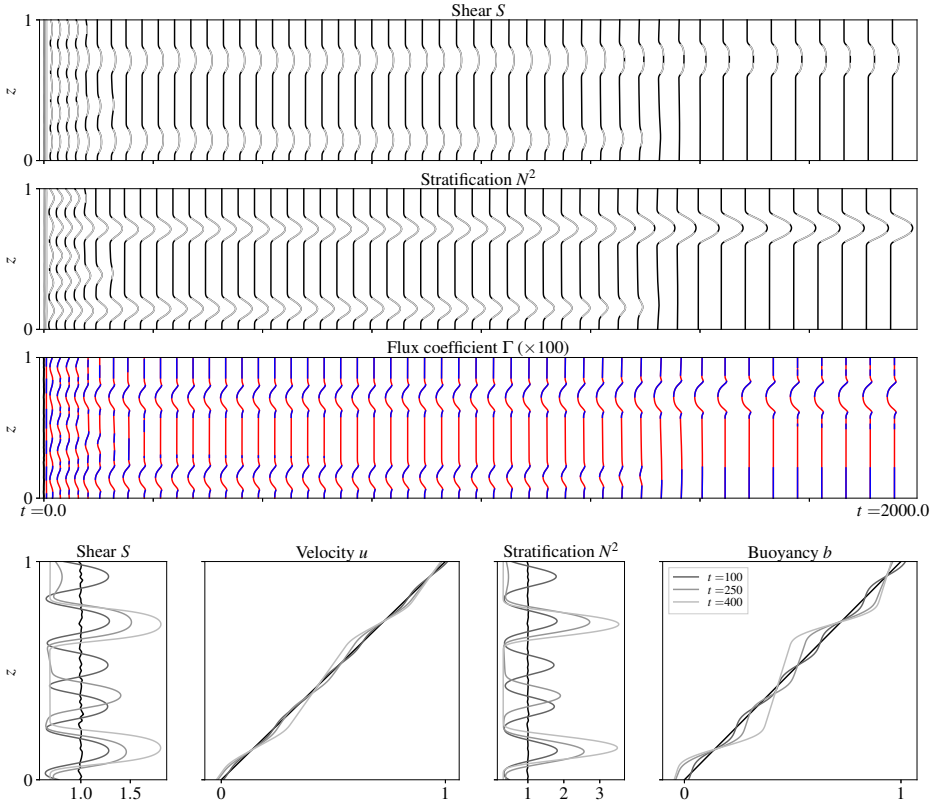


Figure 16: Further late time evolution for case 4 as shown in figure 14. On the top three panels, the horizontal axis is time and each profile is separated by 40 dimensionless time unit. On the buoyancy profiles, the grey regions correspond to regions where the effective eddy diffusivity defined in appendix A is negative. On the flux coefficient profiles, red corresponds to upwelling while blue corresponds to downwelling.

sufficiently small turbulent Prandtl numbers and moderate to large bulk Richardson numbers. More precisely, for relevant oceanic parameters, layering via the Phillips mechanism is only possible within this model for  $\text{Pr}_T \lesssim 0.5 - 0.7$ . The existence of this upper bound on the turbulent Prandtl number, that importantly has been shown to depend strongly on  $\text{Pr}_m$  and weakly on the precise parameterisation of the turbulent fluxes (in the sense that it depends only on the rate of the decrease of  $\Gamma$  with  $\text{Ri}_b$ ) but not on  $\text{Re}$  (for non-zero values of the molecular diffusivity  $\nu_m$ ) nor on the scaling for the dissipation rate of turbulent kinetic energy, confirms that the Phillips mechanism for layer formation is only valid for small values of  $\text{Pr}_T$  in the presence of both buoyancy- and shear-driven turbulence. It also suggests that layer formation is not favoured in ocean interiors, as empirically observed. Indeed, the turbulent Prandtl number in stably stratified turbulence is usually found to be  $\text{Pr}_T \gtrsim 0.7$  (Venayagamoorthy & Stretch 2010). In the top 2 km of the oceans, observations show  $\text{Pr}_T \sim 1 - 2$  (Salehipour *et al.* 2016). Hence, layer formation is only expected to occur on the increasing left flank of the  $\Gamma$ -curve i.e. for sufficiently small values of  $(\text{Ri}_b < \text{Ri}_b^*)$ . However, as discussed in (Riley & Lelong 2000), oceanic flows are often very strongly stratified, suggesting again that layer formation is not favoured in ocean interiors. Considering further the decreasing right flank of the  $\Gamma$ -curve, as the molecular Prandtl number increases, the upper bound on  $\text{Pr}_T$  increases, favouring layer formation as discussed in Taylor & Zhou (2017). The upper bound on  $\text{Pr}_T$  reaches values of order  $\mathcal{O}(100)$  for  $\text{Pr}_m = 700$  (salty water), consistently with the fact that layer formation has often been observed in laboratory experiments. Finally, in the limit  $\nu_m = 0$  (i.e.  $\text{Re} \rightarrow \infty$ ), the upper bound on  $\text{Pr}_T$  for instability is smaller than  $1/2$ , regardless of the form of  $\Gamma$ . This result, independent of the explicit form of  $\Gamma$ , supports again the fact that density staircases formation is not favoured in ocean interiors.

The nonlinear dynamics following the initial linear instability growth exhibit various interesting properties. For flows with unstable parameters on the decreasing right flank of the  $\Gamma$ -curve, behaviour seems to be divided into two categories. For flows with parameters such that  $\Delta > 0$  (see section 4) a layer instability appears to develop simultaneously in both the buoyancy and velocity fields which forms layers that pulse and merge as time evolves. Conversely, for flows with parameters such that  $\Delta \leq 0$  staircases appear to develop first in the buoyancy field, reminiscent of the purely buoyancy-driven mechanism that occurs for  $\text{Pr}_T = 0$ , a case that is equivalent to the Phillips mechanism and for which the instability is also associated with the condition  $\Delta \leq 0$  (section 3.4.3). Moreover, in this case layers merge but do not pulse as the instability saturates. More generally, the nonlinear evolution of the layers underlines the qualitative differences between the mixing expected in the presence or absence of density staircases. In the absence of density staircases, the mixing is purely diffusive in the sense that it smooths density gradients and can be modeled by an appropriately defined (positive) eddy diffusivity (see appendix A). On the contrary, the interfaces between layers are characterised by a negative effective eddy diffusivity and the mixing process at hand scours density interfaces, sharpens density gradients and hence is in some sense ‘antidiffusive’. Since antidiffusive problems are both mathematically and numerically challenging, this raises intricate parameterisation issues for flux-gradient based models. Finally, our model is relevant to ocean interiors where double-diffusive effects are negligible but breaks down near boundaries where boundary effects might become important or in regions of the world’s oceans where double-diffusion becomes prominent such as in polar regions or the Mediterranean Sea.

There are of course several limitations of our model. Firstly, it is important to remember that  $\Gamma$  cannot be parameterised in terms of the Richardson number only. It depends on other parameters, such as the buoyancy Reynolds number  $\text{Re}_b = \epsilon/(\nu_m N^2)$  (Salehipour *et al.* 2016; Mashayek *et al.* 2017). Secondly, our analysis has considered ranges of parameters prone to layer formation provided they can sustain turbulence (so that the considered scalings for  $\epsilon$

hold). We however did not assess whether the full parameter space considered here could actually maintain turbulence. However, the robustness of our results with regard to various scalings for  $\epsilon$  (section 2.2.2) suggests that the model presented here is relevant to both shear-dominated and buoyancy-dominated turbulent regimes (Mater & Venayagamoorthy 2014) as well as in weakly and strongly stratified regimes (Garanaik & Venayagamoorthy 2019).

**Acknowledgements.** For the purpose of open access, the authors have applied a Creative Commons Attribution (CC BY) licence to any Author Accepted Manuscript version arising from this submission.

**Funding.** This project has received funding from the European Union's Horizon 2020 research and innovation program under the Marie Skłodowska-Curie grant agreement N°956457. A.M. acknowledges support from National Environmental Research Council (NE/P018319/1).

**Declaration of interests.** The authors report no conflict of interest.

**Author ORCID.** C. P. Caulfield, <https://orcid.org/0000-0002-3170-9480>

## Appendix A.

Similarly to what we have done in section 3.2, we recast the full (nonlinear) problem (2.8) as a diffusion problem. To do so, note that it can be put into the following matrix form:

$$\begin{bmatrix} \partial_t b \\ \partial_t u \end{bmatrix} = \mathbf{D}_{nl} \begin{bmatrix} \partial_{zz} b \\ \partial_{zz} u \end{bmatrix}, \quad (\text{A } 1)$$

where:

$$\mathbf{D}_{nl} = \begin{bmatrix} \frac{\Gamma'(\text{Ri}_b \text{Ri})}{(\partial_z u)^2} + \frac{1}{\text{Pr}_m \text{Re}} & -2 \frac{\Gamma'(\text{Ri}_b \text{Ri}) \text{Ri}}{\partial_z u} \\ \frac{\text{Pr}_T}{\text{Ri}_b \text{Ri}^2 (\partial_z u)^3} [\text{Ri}_b \text{Ri} \Gamma'(\text{Ri}_b \text{Ri}) - \Gamma(\text{Ri}_b)] & \frac{\text{Pr}_T}{\text{Ri}_b \text{Ri} \partial_z u} [-2 \text{Ri}_b \text{Ri} \Gamma'(\text{Ri}_b) + \Gamma(\text{Ri}_b)] + \frac{1}{\text{Re}} \end{bmatrix}. \quad (\text{A } 2)$$

The matrix  $\mathbf{D}_{nl}$  is the nonlinear diffusion matrix associated to our problem. The real part of the eigenvalues of this matrix can be interpreted as effective eddy diffusivities of the system. Since the sign of these real parts is related to the sign of the trace  $\text{Tr}(\mathbf{D}_{nl})$  and determinant  $\det(\mathbf{D}_{nl})$  of  $\mathbf{D}_{nl}$ , regions where  $\text{Tr}(\mathbf{D}_{nl}) < 0$  or  $\det(\mathbf{D}_{nl}) < 0$  will be prone to antidiffusive dynamics that will sharpen density interfaces. Note that  $-f$  and  $-C$  are the zero-th order approximation of these quantities, linking the linear dynamics to the nonlinear dynamics.

## Appendix B.

Let us formally write the system of equations (4.2) in the following form:

$$\partial_t y = \partial_{zz} [f(y)] - \hat{\kappa}_4 \partial_z^4 y. \quad (\text{B } 1)$$

We first discretize the above in space using second order in space schemes and obtain:

$$\partial_t y_i = \frac{1}{dz^2} [f(y_{i+1}) - 2f(y_i) + f(y_{i-1}))] + \frac{1}{dz^4} [y_{i+2} - 4y_{i+1} + 6y_i - 4y_{i-1} + y_{i-2}], \quad (\text{B } 2)$$

where  $i \in \{2, \dots, N-2\}$  are the indices of the grid points,  $dz$  is the spacing between grid points and  $\mathbf{y}(t) = (y_0(t), \dots, y_N(t))^T$  are the approximate values of  $y(t)$  at the grid points. The formulae for  $i \in \{0, 1, N-1, N\}$  depend on the boundary conditions used in  $z = 0$  and  $z = 1$ . We have considered periodic boundary conditions in our analysis. The above can be put into a matrix form:

$$\partial_t \mathbf{y} = \mathbf{A}_{dz}(\mathbf{y}), \quad (\text{B } 3)$$

with  $\mathbf{A}_{dz} : \mathbb{R}^{N+1} \rightarrow \mathcal{M}^{N+1, N+1}(\mathbb{R})$ . This is a system of  $N + 1$  ODEs. We can now use an appropriate time-stepping scheme to solve the problem numerically. We have used the BDF method with adaptive step-size from the python library `scipy` in order to resolve accurately the stiff dynamics that appear as layers form.

As layers form, the shear  $S$  might become close to zero. This can introduce inappropriate divisions by zero in the definition of the Richardson number and lead to numerical difficulties. To avoid this issue, we consider  $\hat{\text{Ri}} = \frac{\hat{N}^2}{S^2 + \eta}$  where  $\eta$  is a small parameter. We use  $\eta = 10^{-9}$  in our simulations.

## REFERENCES

- BALMFORTH, NJ, SMITH, STEFAN G LLEWELLYN & YOUNG, WR 1998 Dynamics of interfaces and layers in a stratified turbulent fluid. *Journal of Fluid Mechanics* **355**, 329–358.
- BARENBLATT, GI, BERTSCH, M, DAL PASSO, R, PROSTOKISHIN, VM & UGHI, MAURA 1993 A mathematical model of turbulent heat and mass transfer in stably stratified shear flow. *Journal of Fluid Mechanics* **253**, 341–358.
- BILLANT, PAUL & CHOMAZ, JEAN-MARC 2001 Self-similarity of strongly stratified inviscid flows. *Physics of fluids* **13** (6), 1645–1651.
- BOUFFARD, DAMIEN & BOEGMAN, LEON 2013 A diapycnal diffusivity model for stratified environmental flows. *Dynamics of Atmospheres and Oceans* **61**, 14–34.
- CAULFIELD, C.P. 2021 Layering, instabilities, and mixing in turbulent stratified flows. *Annual Review of Fluid Mechanics* **53** (1), 113–145, arXiv: <https://doi.org/10.1146/annurev-fluid-042320-100458>.
- COPE, LAURA, GARAUD, P. & CAULFIELD, C. P. 2020 The dynamics of stratified horizontal shear flows at low péclet number. *Journal of Fluid Mechanics* **903**, A1.
- GARANAİK, AMRAPALLI & VENAYAGAMOORTHY, SUBHAS K 2019 On the inference of the state of turbulence and mixing efficiency in stably stratified flows. *Journal of Fluid Mechanics* **867**, 323–333.
- GARAUD, P, MEDRANO, M, BROWN, JM, MANKOVICH, C & MOORE, K 2015 Excitation of gravity waves by fingering convection, and the formation of compositional staircases in stellar interiors. *The Astrophysical Journal* **808** (1), 89.
- IVEY, GREGORY, IMBERGER, JORG & KOSEFF, J.R. 1998 *Buoyancy fluxes in a stratified fluid*, *Coastal and Estuarine Studies*, vol. 54, pp. 377–388. United States: American Geophysical Union.
- IVEY, G. N. & IMBERGER, J. 1991 On the nature of turbulence in a stratified fluid. part i: The energetics of mixing. *Journal of Physical Oceanography* **21** (5), 650 – 658.
- KAY, DAVID J. & JAY, DAVID A. 2003 Interfacial mixing in a highly stratified estuary 1. Characteristics of mixing. *Journal of Geophysical Research (Oceans)* **108** (C3), 3072.
- KRANENBURG, C 1980 On the stability of turbulent density-stratified shear flow. *Journal of Physical Oceanography* **10** (7), 1131–1133.
- LINDEN, P. F. 1979 Mixing in stratified fluids. *Geophysical & Astrophysical Fluid Dynamics* **13** (1), 3–23, arXiv: <https://doi.org/10.1080/03091927908243758>.
- LINDEN, P. F. 1980 Mixing across a density interface produced by grid turbulence. *Journal of Fluid Mechanics* **100** (4), 691–703.
- MA, YUCHEN & PELTIER, W. R. 2021 Gamma instability in an inhomogeneous environment and salt-fingering staircase trapping: Determining the step size. *Phys. Rev. Fluids* **6**, 033903.
- MASHAYEK, A, SALEHIPOUR, H, BOUFFARD, D, CAULFIELD, CP, FERRARI, R, NIKURASHIN, M, PELTIER, WR & SMYTH, WD 2017 Efficiency of turbulent mixing in the abyssal ocean circulation. *Geophysical Research Letters* **44** (12), 6296–6306.
- MATER, BENJAMIN D & VENAYAGAMOORTHY, SUBHAS KARAN 2014 A unifying framework for parameterizing stably stratified shear-flow turbulence. *Physics of Fluids* **26** (3), 036601.
- OGLETHORPE, RLF, CAULFIELD, CP & WOODS, ANDREW W 2013 Spontaneous layering in stratified turbulent Taylor–couette flow. *Journal of Fluid Mechanics* **721**.
- OSBORN, TR 1980 Estimates of the local rate of vertical diffusion from dissipation measurements. *Journal of physical oceanography* **10** (1), 83–89.
- PHILLIPS, OM 1972 Turbulence in a strongly stratified fluid—is it unstable? In *Deep Sea Research and Oceanographic Abstracts*, , vol. 19, pp. 79–81. Elsevier.

- POSMENTIER, ERIC S 1977 The generation of salinity finestructure by vertical diffusion. *Journal of Physical Oceanography* **7** (2), 298–300.
- RADKO, TIMOUR 2014 Applicability and failure of the flux-gradient laws in double-diffusive convection. *Journal of Fluid Mechanics* **750**, 33–72.
- RADKO, TIMOUR 2016 Thermohaline layering in dynamically and diffusively stable shear flows. *Journal of Fluid Mechanics* **805**, 147–170.
- RADKO, TIMOUR 2019 Thermohaline layering on the microscale. *Journal of Fluid Mechanics* **862**, 672–695.
- RILEY, JAMES J & LELONG, MARIE-PASCALE 2000 Fluid motions in the presence of strong stable stratification. *Annual review of fluid mechanics* **32** (1), 613–657.
- RIPPETH, TOM & FINE, ELIZABETH 2022 Turbulent mixing in a changing arctic ocean. *Oceanography*.
- RUDDICK, BR, MCDUGALL, TJ & TURNER, JS 1989 The formation of layers in a uniformly stirred density gradient. *Deep Sea Research Part A. Oceanographic Research Papers* **36** (4), 597–609.
- SALEHIPOUR, H, PELTIER, WR, WHALEN, CB & MACKINNON, JA 2016 A new characterization of the turbulent diapycnal diffusivities of mass and momentum in the ocean. *Geophysical Research Letters* **43** (7), 3370–3379.
- SHIH, LUCINDA H., KOSEFF, JEFFREY R., IVEY, GREGORY N. & FERZIGER, JOEL H. 2005 Parameterization of turbulent fluxes and scales using homogeneous sheared stably stratified turbulence simulations. *Journal of Fluid Mechanics* **525**, 193–214.
- TAYLOR, J. R. & ZHOU, Q. 2017 A multi-parameter criterion for layer formation in a stratified shear flow using sorted buoyancy coordinates. *Journal of Fluid Mechanics* **823**, R5.
- THORPE, S. A. 1982 On the layers produced by rapidly oscillating a vertical grid in a uniformly stratified fluid. *Journal of Fluid Mechanics* **124**, 391–409.
- THORPE, S. A. 2005 *The Turbulent Ocean*. Cambridge University Press.
- TIMMERMANS, M-L, TOOLE, J, KRISHFIELD, R & WINSOR, P 2008 Ice-tethered profiler observations of the double-diffusive staircase in the canada basin thermocline. *Journal of Geophysical Research: Oceans* **113** (C1).
- TURNER, J. S. 1968 The influence of molecular diffusivity on turbulent entrainment across a density interface. *Journal of Fluid Mechanics* **33** (4), 639–656.
- VENAYAGAMOORTHY, SUBHAS K & STRETCH, DEREK D 2010 On the turbulent prandtl number in homogeneous stably stratified turbulence. *Journal of Fluid Mechanics* **644**, 359–369.
- WELLS, MATHEW, CENEDESE, CLAUDIA & CAULFIELD, C. P. 2010 The relationship between flux coefficient and entrainment ratio in density currents. *Journal of Physical Oceanography* **40** (12), 2713 – 2727.
- WOODS, ANDREW W, CAULFIELD, CP, LANDEL, JULIEN R & KUESTERS, A 2010 Non-invasive turbulent mixing across a density interface in a turbulent taylor–couette flow. *Journal of fluid mechanics* **663**, 347–357.